
EXPLORING SCALABLE MEDICAL IMAGE ENCODERS BEYOND TEXT SUPERVISION

Fernando Pérez-García^{*,1}, Harshita Sharma^{*,1}, Sam Bond-Taylor^{*,1}, Kenza Bouzid¹, Valentina Salvatelli¹, Maximilian Ilse¹, Shruthi Bannur¹, Daniel C. Castro¹, Anton Schwaighofer¹, Matthew P. Lungren², Maria Wetscherek^{1,4}, Noel Codella³, Stephanie L. Hyland¹, Javier Alvarez-Valle¹, and Ozan Oktay¹

¹Health Futures, Microsoft Research

²Microsoft Health and Life Sciences

³Microsoft Azure AI

⁴Department of Radiology, University of Cambridge and Cambridge University Hospitals NHS Foundation Trust, Cambridge, UK

ABSTRACT

Language-supervised pre-training has proven to be a valuable method for extracting semantically meaningful features from images, serving as a foundational element in multimodal systems within the computer vision and medical imaging domains. However, the computed features are limited by the information contained in the text, which is particularly problematic in medical imaging, where the findings described by radiologists focus on specific observations. This challenge is compounded by the scarcity of paired imaging–text data due to concerns over leakage of personal health information. In this work, we fundamentally challenge the prevailing reliance on language supervision for learning general-purpose biomedical imaging encoders. We introduce RAD-DINO, a biomedical image encoder pre-trained solely on unimodal biomedical imaging data that obtains similar or greater performance than state-of-the-art biomedical language-supervised models on a diverse range of benchmarks. Specifically, the quality of learned representations is evaluated on standard imaging tasks (classification and semantic segmentation), and a vision–language alignment task (text report generation from images). To further demonstrate the drawback of language supervision, we show that features from RAD-DINO correlate with other medical records (e.g., sex or age) better than language-supervised models, which are generally not mentioned in radiology reports. Finally, we conduct a series of ablations determining the factors in RAD-DINO’s performance; notably, we observe that RAD-DINO’s downstream performance scales well with the quantity and diversity of training data, demonstrating that image-only supervision is a scalable approach for training a foundational biomedical image encoder.

Model weights of RAD-DINO trained on publicly available datasets and detailed instructions to use are available at <https://huggingface.co/microsoft/rad-dino>.

1 Introduction

In the evolving landscape of vision–language deep learning, the prevalent use of textual supervision [1, 2] has been a cornerstone in learning novel visual descriptors for downstream applications [2, 3], including biomedical domains [4, 5, 6, 7]. With the emergence of large language models (LLMs), these visual descriptors are increasingly being integrated as static input tokens for multimodal reasoning to perform visual question answering (VQA) and text captioning tasks [8, 9, 10].

As the focus shifts towards achieving state-of-the-art (SOTA) performance with larger-scale datasets and models [11], the scalability of models to larger datasets, along with the availability of high-quality datasets, have become increasingly

*Equal contribution. Corresponding authors: fernando.perezgarcia@microsoft.com, harshita.sharma@microsoft.com

vital [12, 13]. However, this shift presents practical challenges in domain-specific applications such as healthcare, particularly in the context of acquisition and curation of large-scale datasets of image–text pairs. Limited availability of public multimodal medical datasets and concerns around the anonymity of protected health information (PHI) hinder the research community’s efforts to scale up medical foundation models. Moreover, the lack of pixel-level supervision, particularly when text data for image segmentation is not available, presents also a substantial challenge. This absence of detailed textual annotations impedes the improvement of image encoders’ performance in tasks demanding precise image analysis, such as the detection and localisation of nodules in 2D or 3D medical scans.

Furthermore, textual supervision may sometimes be limiting, especially when captions lack detail. This is particularly true if radiological findings, which describe key observations about target classes, are omitted. This limitation may lead to a collapse of representations at the expense of image–text alignment [14, 15, 16], where intra-class variations may not be preserved. Specifically for radiology reports, not all the visual details in the image are captured in the text, and absent or negative findings in the image are often mentioned. For instance, the radiological phrase “No cardiopulmonary process” is frequently used to report healthy chest X-rays in the MIMIC-CXR [17] dataset. Hence, its contrastive alignment [18, 19] with image features might introduce undesired invariances to anatomical variations seen across individuals. However, these visual details could be valuable for clinical applications beyond standard text generation, such as image segmentation, or biomarker discovery for therapeutics that require understanding each individual’s uniqueness [20, 21]. Without this context, the applicability of learnt image encoders may not generalise to broader healthcare applications, eventually needing re-training of networks. Indeed, a recent study [15] has demonstrated that, whilst image–text data can be leveraged to establish correspondences between language and the visual world, they may not be precise and clean enough to result in SOTA image descriptors for downstream vision tasks. In a similar direction, we explore the hypothesis that there may not be a need for text supervision to learn discriminative visual descriptors required for uni- and multimodal medical applications: the alignment across the two modalities can be performed subsequently depending on the downstream application, once the visual clustering of features has been performed using large-scale imaging data alone.

For this purpose, we propose RAD-DINO (Fig. 1), an image encoder continually pre-trained with medical scans by adopting the DINOv2 image-only self-supervised learning (SSL) approach [22]. We assess RAD-DINO’s scalability with pre-training dataset size to downstream uni- and multimodal applications including both image- and pixel-level predictive tasks. DINOv2 leverages two complementary training objectives: masked image modelling (MIM) and self-supervised instance discrimination. This hybrid design enables the transferability of learned features to both global and local downstream tasks without requiring external text supervision [23, 24, 25]. In particular, we empirically verify the aforementioned hypothesis by benchmarking RAD-DINO against a series of SOTA baseline image encoders, trained with text supervision, on multiple medical datasets. On image classification, we demonstrate that similar performance levels can be consistently achieved or even surpassed for most of the classes without the need for paired image–text datasets for training (Section 2.1). These findings are generalised to downstream multimodal applications where image-to-text generation results are evaluated with frozen image backbone networks (Section 2.2). We also demonstrate promising semantic segmentation performance, without using a hierarchical encoder architecture such as U-Net [26] or Swin Transformer [27], by training off-the-shelf decoder heads [28, 29] on top of pre-trained RAD-DINO encoders, highlighting the reduced need for large-scale, densely annotated training datasets (Section 2.3). Finally, we show that patient demographic information, which in general is not mentioned in text, can be more accurately predicted from RAD-DINO’s encodings than language supervised models, suggesting that image-only models such as RAD-DINO are more useful for broader clinical applications (Section 3.6).

A series of ablations are conducted to understand the contribution of each component of RAD-DINO to its performance, including: (I) the beneficial impact of domain-transfer with pre-trained weights from DINOv2, (II) the essential role of MIM for image segmentation, and (III) the importance of input image resolution for detecting classes which require fine-grained visual details. Lastly, we analyse how RAD-DINO scales with large and diverse image-only datasets, as this can enable a unified approach without reliance on hand-crafted SSL pretext tasks proposed for specific medical imaging modalities [30, 31].

In summary, our main contributions are as follows:

- We show that supervision with text data is not essential, and it could even hinder learning visual features required for downstream multimodal biomedical applications. Instead, one could employ self-supervision with imaging data only, as we do with RAD-DINO, to achieve comparable or better performance and further scale by leveraging the vast availability of imaging data. RAD-DINO is trained with 838k images and scalable to more image-only data as these become available.
- We demonstrate through a set of ablations that RAD-DINO’s performance scales with increased training dataset size, diversity, and higher input resolution, paving the way for a viable solution to train large-scale foundational biomedical image encoders.

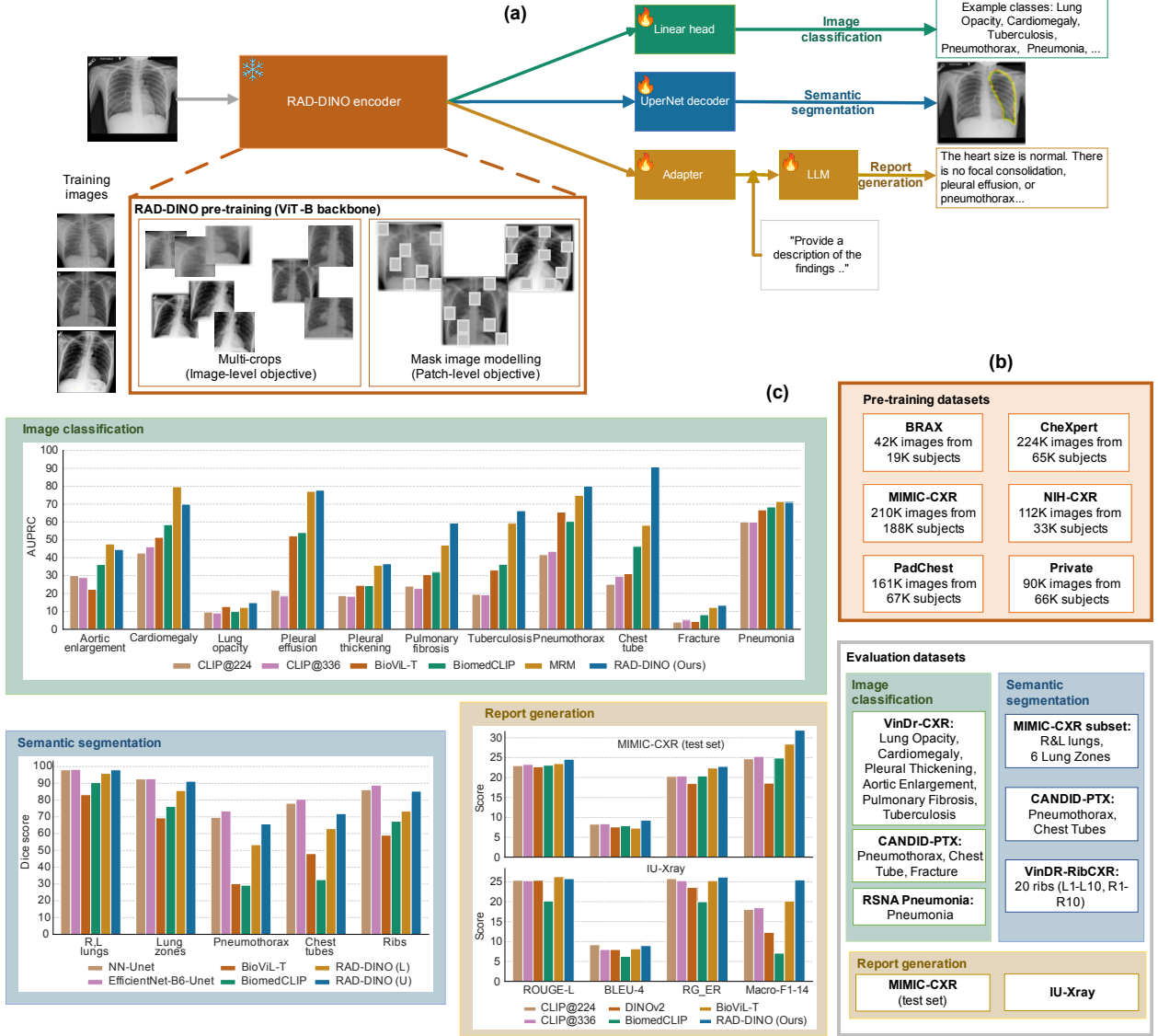


Figure 1: RAD-DINO overview. (a) Model architecture highlighting the training process using image-level and patch-level objectives, and pre-trained RAD-DINO encoder applied on downstream tasks by training task-specific heads. (b) Summary of pre-training and evaluation datasets. (c) Summary of results for image classification (Tables 1a and 1b), semantic segmentation (Table 3) and report generation (Table 2) downstream tasks. RAD-DINO (L) and RAD-DINO (U) refer to linear and UPerNet decoder segmentation heads, respectively.

- We show that RAD-DINO’s features show a stronger correlation with clinical information, e.g., patient medical records, which extends beyond the data typically found in radiology reports yet is routinely relied upon for diagnostic purposes. This capability could enable future multimodal applications that include electronic health records (EHR) data.

Table 1: Image classification results on VinDr-CXR, CANDID-PTX and RSNA-Pneumonia. Results are averaged across five runs with different random seeds.

(a) Image classification results obtained on the VinDr-CXR dataset benchmark (1500 train and 3000 test images, respectively) with linear probing with frozen backbone networks. We report mean and standard deviation AUPRC. RAD-DINO outperforms all the other models on aggregate. Notably, RAD-DINO outperforms bigger models trained on 10 or even 100 times more data (Table 4).

Model	Arch.	VinDr-CXR [35] (AUPRC)								Agg.
		LO	CM	PL-T	AE	PF	TB	PE		
CLIP@224 [2]	ViT-L	9.7 ± 0.4	42.6 ± 0.2	18.8 ± 0.4	30.0 ± 0.5	24.1 ± 0.4	19.6 ± 0.5	21.8 ± 0.4	23.8	
CLIP@336 [2]	ViT-L	9.1 ± 0.1	46.1 ± 0.2	18.5 ± 0.2	29.0 ± 0.3	22.8 ± 0.3	19.4 ± 0.4	18.6 ± 0.3	23.4	
BioViL-T [36]	ResNet50	12.7 ± 0.1	51.4 ± 0.5	24.6 ± 0.2	22.3 ± 0.1	30.5 ± 0.1	33.1 ± 0.2	52.2 ± 0.4	32.4	
BiomedCLIP [37]	ViT-B	10.0 ± 0.3	58.5 ± 0.8	24.4 ± 0.5	36.2 ± 0.2	32.0 ± 0.6	36.3 ± 0.9	54.1 ± 0.6	35.9	
CheXzero [38]	ViT-B	11.1 ± 0.6	74.4 ± 0.2	25.1 ± 0.3	42.9 ± 0.2	33.1 ± 0.4	33.5 ± 0.3	60.2 ± 0.5	40.0	
MRM [7]	ViT-B	12.2 ± 0.3	79.7 ± 0.4	35.8 ± 0.8	47.7 ± 0.6	47.1 ± 0.5	59.3 ± 1.0	77.2 ± 0.3	51.3	
RAD-DINO	ViT-B	14.9 ± 0.2	69.9 ± 0.3	36.6 ± 0.6	44.6 ± 0.3	59.4 ± 0.2	66.3 ± 0.3	77.8 ± 0.4	52.8	

LO: Lung Opacity, CM: Cardiomegaly, PL-T: Pleural Thickening, AE: Aortic Enlargement,
PF: Pulmonary Fibrosis, TB: Tuberculosis, PE: Pleural Effusion, Agg.: Macro average

(b) Image classification results obtained on the CANDID-PTX (60/20/20 split by subject) and RSNA-Pneumonia (60/20/20 split by subject) benchmarks with linear probing with frozen backbone networks. We report AUPRC results collected on the test sets (RSNA-Pneumonia: 5337 images) and (CANDID-PTX: 3833 images). RAD-DINO outperforms all the other models on CANDID-PTX, with a significant margin on pneumothorax (PTX) and chest tubes.

Model	Architecture	CANDID-PTX [39] (AUPRC)			RSNA-Pneumonia [40]	
		PTX	Chest tube	Rib fracture	AUPRC	AUROC
CLIP@224 [2]	ViT-L	41.7 ± 1.6	25.2 ± 1.0	4.0 ± 1.1	60.1 ± 2.0	83.7 ± 0.7
CLIP@336 [2]	ViT-L	43.6 ± 1.1	29.6 ± 1.7	5.2 ± 2.0	60.0 ± 1.7	84.2 ± 0.4
BioViL-T [36]	ResNet50	65.5 ± 1.5	31.1 ± 3.4	4.3 ± 1.9	66.8 ± 1.5	86.9 ± 0.5
CheXzero [38]	ViT-B	57.5 ± 4.1	42.9 ± 4.5	7.2 ± 2.8	68.9 ± 1.9	87.9 ± 0.4
BiomedCLIP [37]	ViT-B	60.4 ± 2.0	46.4 ± 4.4	8.1 ± 2.5	68.4 ± 1.7	87.5 ± 0.4
MRM [7]	ViT-B	74.9 ± 2.4	58.2 ± 4.9	12.2 ± 7.1	71.4 ± 1.5	89.0 ± 0.5
RAD-DINO	ViT-B	80.1 ± 1.6	90.8 ± 1.6	13.4 ± 4.1	71.0 ± 1.8	88.4 ± 0.6

2 Results

2.1 Evaluating RAD-DINO on image classification benchmarks

2.1.1 Experimental setup

RAD-DINO backbones are evaluated against multimodal (image–text), general-domain, and domain-specific image networks. Linear probing is used to compare different approaches. This assessment aims to determine their top performance within each biomedical benchmark, despite differences in pre-training datasets.

All evaluations were performed on three external chest X-ray (CXR) datasets collected from both out-patient and in-patient settings (VinDr-CXR, CANDID-PTX and RSNA-Pneumonia) and hence suitable to test the generalisation of networks. We did not focus on comparing different image-only SSL methods as recent studies have demonstrated that the combination of MIM [32] and image-only contrastive approaches [33], as in the case of iBOT [34] and DINoV2 [22], lead to SOTA performance.

2.1.2 VinDr-CXR benchmark

For five out of seven pathologies (as well as on average) RAD-DINO outperforms all other methods. Only for “cardiomegaly” (CM) and “aortic enlargement” (AE) do multimodal methods outperform RAD-DINO. We hypothesise that, because the heart and aorta are large structures, with clear borders well described in radiology reports, features learned by multimodal methods are more likely to be useful to detect CM or AE, compared to lower contrast and texture-based pathologies.

In general, we find that masked image modelling approaches, including MRM [7], yield stronger performance compared to image–text contrastive-only approaches (Table 1a). However, performance differences between MRM and RAD-DINO are more pronounced on out-of-domain findings, such as chronic or incidental findings in outpatient studies. This is due to the limited availability of multimodal public datasets, with MRM therefore trained solely on MIMIC-CXR [17], which might lack diversity. For instance, the two classes where RAD-DINO exhibits the largest improvement over all other models are PF and TB; a keyword search among all 227.8k study reports in MIMIC-CXR found that both of these are rarely reported (< 1%). In addition, in Appendix B.3 we show that training RAD-DINO with a similar quantity of images to MRM (see Figure B.2), RAD-DINO performs on par with MRM without requiring any text reports. Note that the ablations in [7] show that MRM’s performance relies more on image reconstruction and modelling pretext tasks than text modelling, supporting the thesis that text might not be necessary for strong image representations.

The multimodal baseline results emphasise the importance of data quality and its relevance for downstream tasks. For example, BiomedCLIP [37] was trained with 15 million image–text pairs, retrieved from PubMed articles, 222k of which contained X-rays, and still underperforms RAD-DINO in all benchmarks. RAD-DINO scales well with increasing dataset size and diversity (Appendix B.3), in line with existing literature [41]. Last, we find that the performance of general-domain encoder networks scales with increased capacity and training data [42, 43] as demonstrated by comparing DINOv2 (ViT-G) with DINOv2 (ViT-B) (Table B.1).

2.1.3 CANDID-PTX and RSNA-Pneumonia benchmarks

Linear classification experiments on these two benchmarks (Table 1b) assess the generalisation of models to other external datasets and categorisation of more localised findings (e.g., pneumothorax). Input image resolution plays an important role for CANDID-PTX (Figure C.1). Nevertheless, we observe that RAD-DINO’s 224-pixel version still performs consistently better than image–text contrastive baselines despite the performance drop. The lower AUPRC values for rib fracture are mainly attributed to the availability of fewer positive examples (less than 2%) and the granularity of the finding, which might require encoding images at a very high resolution. On the RSNA-Pneumonia dataset, RAD-DINO performs on par with the SOTA, despite not requiring text supervision. The lack of notable improvement over baselines may stem from the abundance of opacities and pneumonia-related images in public datasets, leading to a narrow performance gap.

2.1.4 Lateral CXR scans

Only frontal chest X-rays are used in the previous classification experiments. However, lateral scans capture certain abnormalities better than frontal scans and are therefore also commonly used to disambiguate findings, with the same text report used for both images. The fact that many written findings are not clearly visible in the lateral scan [44, 45] substantially reduces the mutual information and adds noise to the learning process, making language-supervised methods less effective. We investigate this hypothesis by training a linear classifier to detect abnormalities visible only in lateral scans and observe that the approaches based on MIM (RAD-DINO and MRM) substantially outperform the CLIP-style models (Table C.1).

2.1.5 Impact of learning objectives

RAD-DINO is observed to pick up local textures (see the self-attention maps in Figure C.3), which we attribute to both MIM [34] and multi-crop instance discrimination training [46]. Similarly, correspondences between patch embeddings across scans from different subjects where pathological semantics are captured during training (Figure 2, and Appendix C.5 for additional examples showing matches between findings and anatomical landmarks). [25] show that DINO benefits from its multi-crop training setup as it is specifically trained to be invariant to both local and global scale of structures, and [24] emphasise the importance of MIM in learning high-frequency information present in images whilst contrastive objectives favour learning global-shape representations. In the pneumonia linear-probing task, we observed for CLIP-style backbones a warm start and faster convergence, possibly due to the widespread availability of pneumonia-associated image findings (e.g., opacities) in public benchmarks and their detailed descriptions in radiology reports. This availability likely contributes to the narrower performance gap observed between different baselines.

2.2 Evaluating RAD-DINO for report generation from images

2.2.1 Experimental setup

CLIP-style multimodal pre-training [2] aims for symmetrical alignment between image and text embeddings. Here we investigate whether this procedure is required for a vision–language downstream task, namely generation of the *Findings* section of a frontal chest X-ray report. For this, we use the MIMIC-CXR dataset [17], following the official test and

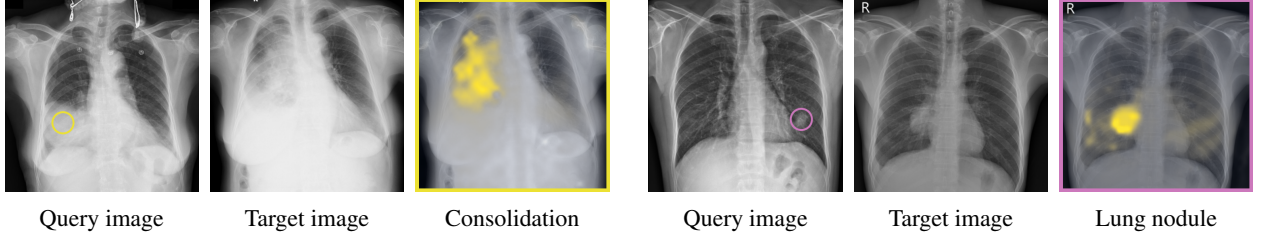


Figure 2: Visual token embedding similarities between pairs of chest X-ray images, computed with RAD-DINO, are shown with respect to a token marked on each query image with a circle. The two manually-picked query tokens (in yellow, left, and purple, right) highlight consolidation and a lung nodule, respectively. For each query token, its similarity to the token embeddings of the target image is highlighted in yellow and is proportional to the heatmap brightness. RAD-DINO can match findings across images from different subjects, thanks to the features learnt during SSL training.

train splits in alignment with data used for RAD-DINO, removing all non-frontal scans, and dropping samples without a *Findings* section, resulting in 146,909 / 7,250 / 2,461 image–text pairs for training, validation, and testing, respectively, for fine-tuning the language decoder. We also evaluate the report generation performance on the IU-Xray [47] dataset, which was not used to train the image encoder nor the language decoder. The MRM baseline [7] is excluded from this analysis as the backbone network was trained with the complete set of image-text pairs in MIMIC-CXR.

We follow a LLaVA-style architecture [48, 49] to produce a multimodal model. Patch embeddings from the frozen image encoder are projected and concatenated with an instruction to generate an output report: “*<image_tokens> Provide a description of the findings in the radiology image.*” Following LLaVA-1.5 [49], we use a two-layer fully connected (MLP) projector and Vicuna-7B (v1.5) [50] as the language model. The projection network is initialised with random weights and trained with the decoder model, whilst the image encoder is frozen. Input information to the LLM is kept minimal to focus evaluation on the quality of the image representations. Further performance gains might be obtained by applying data augmentation [51] or providing additional clinical information, including prior reports [36], but this is out of the scope of this study.

We report standard lexical metrics (ROUGE-L [52], BLEU-4 [53]) to measure word overlap of the generated findings and corresponding ground-truth findings sections, in addition to the radiology-specific RGER [54] and CheXbert-based [55] Macro-F1-14 [56] (with the ‘uncertain’ label mapped as negative). The Macro-F1-14 metric measures the factuality of reported findings for 14 different classes.

2.2.2 Results analysis

RAD-DINO surpasses all other image encoders at every lexical and clinical metric for MIMIC-CXR (Table 2(a)), and all but one lexical metric for IU-Xray (Table 2(b)) for the report generation task. We observe significant improvements over the specialised baselines (BiomedCLIP, BioViL-T and ChexZero), which are pre-trained with language supervision. The large increase in Macro-F1-14 indicates that the embeddings provided by RAD-DINO effectively capture the relevant pathologies, producing more factually correct reports. These results highlight the effectiveness of DINOv2-style image-only pre-training, which learns the relevant features required for generating accurate description of findings of CXR. These results also add weight to the findings in [57] that image resolution is more important than the number of tokens, indicating that increasing resolution might improve scalability.

2.2.3 Balancing training datasets

To assess the importance of training on in-domain data, we carry out a controlled experiment (referred to as RAD-DINO-Control in Table 2), training solely on MIMIC-CXR, a smaller set of the in-domain data used in this study, which was also used to train BioViL-T. RAD-DINO also outperforms other encoders in this scenario, indicating that the improvement over baselines is not merely due to training on extensive radiology data, but rather inherent to the effectiveness of the method. We observe a minimal gap between the control and all-data regimes, likely because the train and test data of the control model come from the same distribution (i.e., MIMIC-CXR). Overall, these results suggest RAD-DINO is a strong encoder option for downstream vision–language tasks in the radiology domain.

Table 2: Downstream radiology report generation results. The same set of image encoders are used in conjunction with a two-layer MLP projector and the Vicuna-7B (v1.5) [50] LLM to generate the *Findings* section from the given input images. We report median and 95% confidence intervals from 500 bootstrap samples.

(a) Results for the official test split of MIMIC-CXR ($N = 2461$).

Image encoder	Input resolution	# of Tokens	ROUGE-L	BLEU-4	RG_{ER}	Macro-F1-14
CLIP@224 [2]	224×224	256	23.0 [22.7, 23.4]	8.3 [7.9, 8.6]	20.3 [19.8, 20.7]	24.7 [23.6, 26.0]
CLIP@336 [2]	316×316	576	23.3 [22.9, 23.7]	8.4 [8.0, 8.7]	20.4 [19.9, 20.9]	25.3 [24.2, 26.5]
DINOv2 [22]	518×518	1369	22.7 [22.4, 23.2]	7.6 [7.3, 7.9]	18.5 [18.1, 19.1]	18.6 [17.8, 19.5]
BiomedCLIP [37]	224×224	256	23.1 [22.8, 23.5]	7.9 [7.5, 8.2]	20.4 [19.9, 20.8]	24.9 [23.8, 26.1]
CheXzero [38]	224×224	49	23.2 [22.9, 23.6]	8.0 [7.7, 8.4]	20.6 [20.2, 21.1]	26.2 [25.0, 27.5]
BioViL-T [36]	512×512	196	23.5 [23.2, 23.9]	7.3 [7.0, 7.6]	22.4 [21.9, 22.8]	28.4 [27.2, 29.8]
RAD-DINO-Control	518×518	1369	24.2 [23.8, 24.6]	9.0 [8.7, 9.4]	22.4 [21.9, 22.9]	31.5 [30.1, 32.9]
RAD-DINO	518×518	1369	24.6 [24.2, 25.0]	9.3 [8.9, 9.7]	22.8 [22.3, 23.3]	31.9 [30.4, 33.3]

(b) Results for IU-Xray ($N = 3306$).

Image encoder	Input resolution	# of Tokens	ROUGE-L	BLEU-4	RG_{ER}	Macro-F1-14
CLIP@224 [2]	224×224	256	25.4 [25.1, 25.7]	9.2 [8.9, 9.5]	25.8 [25.3, 26.2]	18.1 [16.1, 20.8]
CLIP@336 [2]	316×316	576	25.3 [24.9, 25.6]	8.0 [7.8, 8.3]	25.3 [24.8, 25.6]	18.5 [16.7, 20.8]
DINOv2 [22]	518×518	1369	25.4 [25.1, 25.7]	8.0 [7.7, 8.2]	23.6 [23.2, 24.0]	12.3 [10.6, 14.1]
BiomedCLIP [37]	224×224	256	20.2 [19.9, 20.4]	6.3 [6.1, 6.5]	20.0 [19.7, 20.4]	7.1 [5.9, 8.5]
CheXzero [38]	224×224	49	25.6 [25.2, 25.9]	8.5 [8.2, 8.8]	25.7 [25.2, 26.1]	18.1 [16.3, 20.1]
BioViL-T [36]	512×512	196	26.3 [25.9, 26.6]	8.2 [7.9, 8.4]	25.3 [24.9, 25.7]	20.2 [18.0, 23.0]
RAD-DINO-Control	518×518	1369	25.5 [25.2, 25.9]	9.2 [8.9, 9.4]	26.2 [25.8, 26.6]	23.8 [21.4, 26.3]
RAD-DINO	518×518	1369	25.8 [25.4, 26.1]	9.0 [8.8, 9.3]	26.2 [25.7, 26.5]	25.5 [23.0, 28.0]

2.3 Evaluating RAD-DINO on segmentation benchmarks

2.3.1 Experimental setup

To further probe the patch-level representation capabilities of RAD-DINO, we assess its performance on downstream segmentation tasks using common CXR datasets for anatomy or pathology segmentation (CANDID-PTX, and datasets derived from MIMIC-CXR; more details in Appendix D.2). We use each frozen backbone in an encoder-decoder framework with different decoder heads: linear [22], ViTDet [28], and UPerNet [29]. This selection is intended to measure linear discrimination of patch embeddings and their top-level performance using a feature pyramid network (FPN) [58] and a standard vision transformer. We compare with RAD-DINO the same set of backbone networks as in the previous experiments.

Additionally, to understand the potential upper bound on performance [59], we train end-to-end and evaluate U-Net [26] encoder-decoder networks using different image encoders, NN-UNet [60] and EfficientNet-B6 [61], primarily due to their ability to preserve high-resolution spatial information through skip connections between encoder and decoder layers.

2.3.2 Results analysis

Comparison with image-text contrastive methods Image–text CLIP approaches do not yield transferable patch embeddings for downstream segmentation tasks, as the contrastive objective does not necessarily require pixel-level textures to identify correspondences between multimodal instances [24] (Table 3 and Fig. C.6). This is in line with the findings in [22], where the DINOv2 pretrained encoder consistently outperforms the OpenCLIP encoder [62]. The performance gap widens for a fixed type decoder head (linear) as the segmentation task becomes more challenging with smaller target structures such as chest tubes. These results suggest that rich pixel-level features to represent fine-grained image information may not be suitably captured by image–text contrastive training, but are well captured by the RAD-DINO encoder trained using large-scale image-only datasets.

masked image modelling (MIM) matters for biomedical image segmentation By running an ablation on RAD-DINO trained without the MIM objective, we further investigate the complementary nature [24] of the two training objectives discussed in Section 3, where the model is trained only with the instance discrimination term between global

Table 3: Semantic segmentation results obtained with a linear head [22], ViTDet [28], and UPerNet [29] decoders on top of frozen backbone encoders (# Params is the number of trainable parameters). U-Net networks were trained end-to-end to assess the upper-bound performance on a given task. Dice scores are reported as ‘mean (standard deviation)’ across the cases in the dataset with masks. ‘Lungs’ denotes the separate segmentation of the left and right lungs, while ‘Lung zones’ refers to the segmentation of six distinct lung zones as in [63]. The average Dice score across structures is used for both scenarios.

Encoder	Decoder	# Features	# Params	Lungs	Lung zones	Pneumothorax	Chest tubes	Ribs
NN-UNet [60]	Unet	—	17.9 M	98.0 (1.1)	92.6 (10.2)	69.7 (30.2)	78.1 (29.2)	86.2 (2.8)
EfficientNet-B6 [61]	Unet	—	45.9 M	98.3 (1.1)	92.7 (10.1)	73.5 (26.9)	80.5 (27.0)	88.9 (2.6)
BioViL-T [36]	Linear	2048	2049	83.2 (3.2)	69.4 (9.0)	30.2 (28.3)	48.1 (48.0)	59.1 (4.7)
BiomedCLIP [37]	Linear	768	769	90.4 (2.6)	76.2 (10.2)	29.3 (21.7)	32.6 (45.0)	67.4 (4.5)
CheXzero [38]	Linear	768	769	84.0 (3.4)	68.3 (9.1)	21.8 (21.4)	47.7 (49.3)	62.0 (3.3)
RAD-DINO (no MIM)	Linear	768	769	91.3 (2.5)	78.8 (9.6)	35.8 (25.7)	41.3 (42.4)	67.3 (4.7)
RAD-DINO	Linear	768	769	95.9 (1.5)	85.7 (9.8)	53.4 (26.1)	63.0 (39.3)	73.4 (3.6)
RAD-DINO	ViTDet	4×768	24.8 M	97.8 (1.2)	90.7 (10.0)	61.7 (26.2)	54.4 (40.4)	83.6 (2.9)
RAD-DINO	UPerNet	4×768	39.3 M	98.0 (1.1)	91.2 (10.1)	65.8 (28.3)	71.9 (37.1)	85.3 (2.6)

and multi-local crops. The instance discrimination objective focuses on global relationships (e.g., shape), whereas MIM is more inclined towards local relationships (e.g., textures). Thus, especially for dense downstream tasks such as segmentation, MIM could be particularly important. The MIM objective helps boost the segmentation performance for all the structures and datasets (Table 3), showing that MIM contributes to effective representations for our dense tasks.

2.3.3 Role of encoder-decoder choice

Variants of image FPNs [58], including the U-Net approach used to set the performance upper bound, have been consistently applied to dense localisation and segmentation tasks as they efficiently leverage low- and high-level semantic features simultaneously. In that regard, solely using vanilla vision transformers is not an optimal selection for this purpose due to their single-scale feature map throughout the network. Therefore, we combine these encoders with FPN-based decoder heads (e.g., UPerNet) for a fairer comparison.

We observe that pre-training alone is a good candidate for learning transferable frozen features—similarly to how DINOv2 features were shown to perform well out-of-the-box without the need for fine-tuning [22]—and is competitive with end-to-end networks trained specifically for the downstream tasks, such as the U-Net in Table 3 and other recent chest X-ray segmentation models [64, 65, 66, 67]. Similarly, large performance gains are noted for smaller structures with the use of intermediate activations and FPN-based decoder heads. We conjecture that further gains might be achieved by introducing feature pyramids for image encoding, using hierarchical architectures such as Swin Transformers [27].

3 Methods and experimental setup

3.1 DINOv2

In this work we leverage DINOv2, a state-of-the-art image-only self-supervised learning method, optimised for pre-training vision transformers (ViTs) [22]. This approach uses a siamese network [68], with predictions from a teacher network distilled into a student network. To learn image representations useful for both global and localised downstream tasks without requiring text captions, image-level and patch-level objectives are used concurrently [23, 24]. For the patch-level objective, masked image modelling (MIM) is used, where the student is fed an image with randomly masked patches, and must predict the teacher’s features for each patch. For the image-level objective, a contrastive training objective is used: the student is separately fed multiple crops (multi-crop) of an image, and must align its local feature representations with those predicted by the teacher network for the global views of the image. The teacher network is updated through the student’s parameters using exponential moving average (EMA) [69], with gradient back-propagation limited to the student network.

The combination of these objectives plays a key role in DINOv2’s SOTA performance over traditional SSL techniques that rely solely either on contrastive (e.g., CLIP [2], SimCLR [19]) or masked modelling objectives (BEiT [70]). Additionally, the use of multi-crop helps enable resultant backbone networks to learn distinctive local features required for dense predictive tasks [25], e.g., semantic segmentation and depth estimation. To prevent mode collapse, asymmetric

Table 4: Overview of image backbones and their training dataset characteristics employed in experimental analysis

Model type	Model	Arch.	# Params.	Training dataset	# Images	# Text	Image resolution
Image & Text	CLIP@224 [2]	ViT-L/14	304 M	WebImageText	400 M	400 M	224 × 224
Image & Text	CLIP@336 [2]	ViT-L/14	304 M	WebImageText	400 M	400 M	336 × 336
Image & Text	BioViL-T [36]	ResNet50	27 M	MIMIC-CXR	197 k	174 k	512 × 512
Image & Text	BiomedCLIP [37]	ViT-B/16	86 M	PMC-15M	15 M	15 M	224 × 224
Image & Text	CheXzero [38]	ViT-B/32	151 M	MIMIC-CXR	377 k	227 k	224 × 224
Image & Text	MRM [7]	ViT-B/16	86 M	MIMIC-CXR	377 k	227 k	448 × 448
Image Only	DINO-v2 [22]	ViT-G/14	1.1 B	LVD	142 M	-	518 × 518
Image Only	RAD-DINO-Control	ViT-B/14	87 M	MIMIC-CXR	197 k	-	518 × 518
Image Only	RAD-DINO	ViT-B/14	87 M	Multi-CXR	838 k	-	518 × 518

design choices are applied across the two branches, including different augmentation views, centring, and temperature scaling (see [71] for further analysis). The asymmetry in centring techniques contributes to the robustness of the learning process. Furthermore, DINOv2 utilises a KoLeo regulariser [72], which promotes a uniform distribution of features. This is particularly beneficial for clustering-related tasks such as nearest-neighbour image retrieval.

3.2 Training setup

We use a collection of large-scale radiology image-only datasets, namely Multi-CXR, composed of several public and private sources with a wide diversity in terms of findings and demographics (see outline in Table D.1). The pre-trained DINOv2 ViT-B model is continually trained with these CXR images for an additional 60k training steps with a batch size of 640. In contrast to the low-to-high-resolution two-phase learning schedule used in [22], the input resolution is kept the same throughout the training due to the shorter length of our continual training. The dual-view augmentations are adjusted to meet domain-specific requirements, as target classes (disease findings) need texture and contextual information, resulting in larger crop sizes and less severe blurring on the teacher branch (see Appendix E.1). This approach is consistent with the findings in [73] for X-rays and [23] for natural images.

3.3 Baseline approaches

A range of baseline approaches (see Table 4) were selected for experimental analysis, as detailed in Table 4. Specifically, the prevalent use of image-text pairs in CLIP (BioViL-T [36], BiomedCLIP [37] and CheXzero [38]) and multimodal masked modelling (MRM [7]) guided our selection. We primarily aim to investigate the hypothesis that text supervision might not be essential to learn image encoders required for uni- and multi-modal downstream applications. Additionally, this varied selection facilitates the analysis of factors like input image resolution, training dataset size, and the need for domain-specific pre-training. Comparison with image-only SSL methods is left outside the scope of this study as it is extensively studied in prior art [22, 23, 33]. Moreover, evaluating CLIP@336 and CLIP@224 within the same framework highlights the current limitations of medical multimodal learning literature [8, 9], which largely depends on static CLIP-based image encoders. The experiments leveraged publicly available model checkpoints (see Appendix E.2), maintaining consistent train–test splits and evaluation metrics.

3.4 Downstream evaluation tasks

Image-level and pixel-level predictive tasks often necessitate distinct feature invariances [74], thereby requiring complementary pre-training objectives [23, 22]. To evaluate the global and textural characteristics of the learned features, we employ semantic image segmentation and linear probing for image classification tasks with frozen backbone networks, incorporating external datasets and a few long-tail findings (less frequently observed cases). Crucially, we also evaluate the usefulness of learned features for multimodal prediction tasks, namely image-to-text generation; this additionally allows us to determine how well image-only tasks correlate with text-related tasks. For this purpose, Vicuna-1.5 7B LLM [50] is fine-tuned on each frozen image backbone in a LLaVA-style setting [49, 48] (more details in Section 2.2).

3.5 Evaluation datasets and metrics

Across all applications, data splits are carefully constructed to ensure that all the images from each subject (patient) are confined to a single split, thereby preventing potential data leakage. Image classification is evaluated using external

datasets, including VinDr-CXR [35], CANDID-PTX [39], and RSNA-Pneumonia [40]. For VinDr-CXR, a subset of six findings is selected, emphasising diversity (in-/out-patient) and prevalence, given the dataset’s long-tailed distribution. This dataset is particularly used for ablation studies due to its diverse data distribution, including a variety of findings and patient demographics, compared to other public datasets, see Appendix D.2 for further details on the datasets. Results are reported using the AUPRC metric, chosen over AUROC or threshold-dependent accuracy/F1 values due to significant class imbalance. It is noted that target classes are not mutually exclusive. For easier visualisation and comparison, macro AUPRC results are presented in the ablation studies.

In the segmentation tasks, a dedicated decoder head is trained from scratch. Evaluation is performed using Dice scores across various anatomical and pathological classes in chest X-rays, including left and right lungs [75], six lung zones [63], pneumothorax [39], chest tubes [39], and ribs [76]. For more information on their respective datasets, see Appendix D.2. For text report generation, the MIMIC-CXR [17] dataset was exclusively used for training, owing to the scarcity of publicly accessible, large-scale image–text pairs necessary for LLM fine-tuning. Performance is quantified using standard lexical and factuality metrics, and results are reported on the official MIMIC-CXR test split. We also report these metrics on IU-Xray [47] used as an external test dataset.

3.6 RAD-DINO can extract patient demographics

3.6.1 Experimental setup

While patient demographics and medical records such as sex, age, weight, and body mass index (BMI) are not routinely included in chest X-ray reports, they are considered by radiologists during image interpretation, radiation dose decisions [77], and follow-up interventions. However, patients’ demographics are often correlated with imaging features, for example in 3D-tomographic scans, where 2D scout images can provide a useful approximation [78, 79]. We hypothesise that image encoders trained with text-based weak supervision (e.g., BiomedCLIP and BioViL-T) may not capture this patient information, even though it may manifest in the pixel data. We compare the performance of a linear classifier using a frozen RAD-DINO encoder with classifiers on top of frozen BiomedCLIP and BioViL-T encoders. We select a subset of the MIMIC-CXR dataset ($N = 60.1k$) where the radiology reports noted “no findings”. We then link the anonymised subject information with the medical records provided in the MIMIC-IV dataset [80].

Table 5: Linear classification of patients’ demographics with frozen backbone networks. We perform five-fold cross validation and report ‘mean (standard deviation)’ accuracy. While the sex variable is binary, we bin the age (years), weight (kg) and BMI (kg/m^2) variables into five discrete intervals each (Appendix E.3).

Encoder	Sex	Age	Weight	BMI
BioViL-T [36]	75.1 (0.3)	60.8 (0.5)	43.8 (0.5)	47.6 (0.1)
BiomedCLIP [37]	86.0 (0.3)	56.5 (0.5)	52.8 (0.4)	54.2 (0.1)
RAD-DINO	99.6 (0.1)	72.3 (0.3)	62.4 (0.4)	71.3 (0.2)

3.6.2 Results analysis

As shown in Table 5, RAD-DINO significantly outperforms baselines in predicting sex, age, weight, and BMI. This suggests that SSL captures a more comprehensive set of imaging information. It is important to note that differences in image resolution and training data are expected to have less impact on these variables, as global image characteristics (e.g., size of mediastinum, AP/PA view, appearance of bones, and width of fat layer) play a more significant role. While in some applications, invariance to demographics factors such as ethnicity can be a desired attribute to avoid unwanted bias, it is important to consider that other factors, such as age and sex, are commonly used in the clinical decision-making process, and so it is important for an image encoder to capture them. For instance, similar abnormalities may be interpreted differently, and with different levels of concern for different patient age groups. Last, to address concerns about bias in the RAD-DINO features, we perform a stratified analysis of our segmentation and report generation results, see Appendix C.6. We do not observe any signs of decreased fairness in RAD-DINO’s performance compared to the other baseline models.

4 Discussion and conclusion

In this study, we demonstrated that high quality general purpose biomedical image encoders useful for a diverse range of downstream tasks, can be trained solely using unimodal imaging data. This is in contrast to prior state-of-the-art biomedical methods which rely on language supervision. Towards this goal, we developed RAD-DINO by

continually pre-training DINOv2 with domain-specific augmentations and datasets, without specialising on a specific set of modalities or task-specific supervisory objectives, instead using the raw imaging data alone. The experimental results across multiple benchmarks demonstrated that RAD-DINO achieves comparable or superior performance to state-of-the-art methods, a distinction attributed to its independence from text supervision quality and its ability to capture a wider range of imaging features at scale.

To explain RAD-DINO’s performance, we postulated that reliance on additional modalities can not only not be necessary, but actually become a potential limitation in learning rich visual representations of medical scans; in the case of textual reports this depends on their descriptiveness and completeness. Moreover, language supervised models may not generalise beyond the content reported in findings. For instance, by mapping scans without any abnormalities to the same latent representation, CLIP-style image networks can fail to link imaging data with other clinical data modalities, explore new imaging biomarkers, and enable prognosis that require medical scans. Strengthening these findings, we performed a number of ablations where we found that: pre-existing large-scale Vision Transformer-based image encoders with no in-domain biomedical knowledge already generalise surprisingly well to chest X-ray datasets, yielding results that are on par with some established biomedical baselines, echoing findings in [81, 82]; RAD-DINO’s imaging features correlate better with patient medical records than CLIP-style models; and that unlike CLIP-style models, RAD-DINO can naturally handle the challenge of learning from both frontal and lateral scans simultaneously without fusing multiple views or associating textual phrases with each view separately.

A further advantage of the RAD-DINO approach is that it allows the vast amounts of medical imaging-only data to be leveraged, enabling larger-scale models to be trained. This circumvents the well known problems of scarcity of paired image–text pairs in public datasets, while also opening up application areas including histopathology and sonography, where text is rarely available. Relying only on image self-supervision also enables applications with increased resolution and dimension (e.g., full-body 3D CT images); there, the weak supervision signal from text data can become sparse and less reliable, requiring multiple-instance learning or ad-hoc pre-processing solutions, limiting their scalability. For this reason, we conjecture that self-supervised training, using RAD-DINO or other MIM approaches, will scale more easily with the addition of data from other imaging modalities, whilst achieving similar or better results than current SOTA approaches. Additionally, our analysis on input image resolution emphasises the importance of breaking down analysis of results per target class: some subsets of findings require fine-grained analysis of texture; for instance in this work pneumothorax and chest tubes, where RAD-DINO shows no major limitations. The importance of image resolution is expected to be further pronounced in the context of describing attributes of findings, e.g., severity and temporal progression, which is partly quantified within our report generation experiments. However, while demonstrably important, RAD-DINO’s superior performance is not solely attributed to image resolution.

With the growth of large-scale computation and availability of extensive training data, we have begun to witness the potential of large-scale models for tasks beyond their initial scope, able to learn ad-hoc from a few examples [83, 84]. We expect a similar trend to unfold in the medical domain [85]. Our work makes progress in this direction; rather than fine-tuning such large networks for a narrow set of applications, producing multiple resultant encoders, we advocate for reusing them with task-specific heads (e.g., segmentation, language decoding) in different contexts as a more effective and efficient strategy to enable AI solutions in wider healthcare settings. This also requires complementary benchmarking efforts across a broad set of applications, as in the case of our RAD-DINO study, not focusing solely on unimodal evaluations [7, 82] but also including multimodal tasks like textual report generation.

Additionally, to facilitate further research and reproducibility, a model checkpoint trained with the public subset of our training data is publicly available on Hugging Face at <https://huggingface.co/microsoft/rad-dino>. Due to the limited scope of our study, we have not studied alternative encoder architecture adaptions, such as Swin Transformers. However, we expect that using such a multi-scale backbone within our RAD-DINO approach would provide further performance gains for image segmentation, without compromising on performance for the other benchmarks. Similarly, performance of the RAD-DINO image backbone for report generation could be further improved by aggregating intermediate layers and fine-tuning a higher-capacity adaptation layer, as in [86], to better adapt image representations for the LLM. We leave this for the future work.

We recognise that zero-shot image classification and text-to-image retrieval (or vice-versa) is a limitation of RAD-DINO with respect to CLIP-style models such as CheXzero or BioViL-T. However, we believe that RAD-DINO could potentially serve as the image encoder in a CLIP-style model similar to the approach used in [15]; this will be explored in future work to facilitate zero-shot downstream applications. Future work will include exploring additional multimodal tasks in radiology, such as VQA.

5 Data availability

We used a mix of public and private datasets in this study. CheXpert v1.0 is available at <https://stanfordmlgroup.github.io/competitions/chexpert/>. ChestX-ray14 [87], the NIH Chest X-ray Dataset, is available at <https://nihcc.app.box.com/v/ChestXray-NIHCC>. PadChest [88] is available at <https://bimcv.cipf.es/bimcv-projects/padchest/>. USMix is a dataset, with a mix of in-patient and out-patient facilities in the United States, and is not publicly available. VinDR-RibCXR [76] is available at <https://vindr.ai/datasets/ribcxr>. CANDID-PTX [39] is available after completion of an ethics training at <https://doi.org/10.17608/k6.auckland.14173982.v1>. RSNA-Pneumonia [40] is available on Kaggle (<https://www.kaggle.com/c/rsna-pneumonia-detection-challenge>). IU-Xray [47] is available on Kaggle (<https://www.kaggle.com/datasets/raddar/chest-xrays-indiana-university>). The following datasets are available on PhysioNet [89] after a credentialing process: MIMIC-CXR v2.0.0 [17] (<https://doi.org/10.13026/C2JT1Q>), VinDr-CXR [35] v1.0.0 (<https://doi.org/10.13026/3akn-b287>), Chest ImaGenome v1.0.0 [63] (<https://doi.org/10.13026/wv01-y230>), BRAX v1.1.0 [90] (<https://doi.org/10.13026/grwk-yh18>), and the lung segmentations for MIMIC-CXR (v1.0.0) [75] (<https://physionet.org/content/lung-segment-mimic-cxr/1.0.0/>).

6 Code availability

We used the DINOv2 [22] codebase (<https://github.com/facebookresearch/dinov2>) to train RAD-DINO, changing hyperparameters, preprocessing, and augmentation as described in this manuscript, and adding support to train at scale on Azure Machine Learning.

We trained a version of RAD-DINO on publicly available datasets only (i.e., excluding USMix) and share the model on Hugging Face to facilitate further research by the community: <https://doi.org/10.57967/hf/3050>. The release includes the model weights, usage instructions, a model card, and a list of all the image files used for training.

References

- [1] Karan Desai and Justin Johnson. Virtex: Learning visual representations from textual annotations. In *Proceedings of the IEEE/CVF conference on computer vision and pattern recognition*, pages 11162–11173, 2021.
- [2] Alec Radford, Jong Wook Kim, Chris Hallacy, Aditya Ramesh, Gabriel Goh, Sandhini Agarwal, Girish Sastry, Amanda Askell, Pamela Mishkin, Jack Clark, et al. Learning transferable visual models from natural language supervision. In *International conference on machine learning*, pages 8748–8763. PMLR, 2021.
- [3] Jiahui Yu, Zirui Wang, Vijay Vasudevan, Legg Yeung, Mojtaba Seyedhosseini, and Yonghui Wu. Coca: Contrastive captioners are image-text foundation models. *Trans. Mach. Learn. Res.*, 2022, 2022. URL <https://openreview.net/pdf?id=Ee277P3AYC>.
- [4] Benedikt Boecking, Naoto Usuyama, Shruthi Bannur, Daniel C Castro, Anton Schwaighofer, Stephanie Hyland, Maria Wetscherek, Tristan Naumann, Aditya Nori, Javier Alvarez-Valle, et al. Making the most of text semantics to improve biomedical vision–language processing. In *European conference on computer vision*, pages 1–21. Springer, 2022.
- [5] Shih-Cheng Huang, Liyue Shen, Matthew P Lungren, and Serena Yeung. Gloria: A multimodal global-local representation learning framework for label-efficient medical image recognition. In *Proceedings of the IEEE/CVF International Conference on Computer Vision*, pages 3942–3951, 2021.
- [6] Yuhao Zhang, Hang Jiang, Yasuhide Miura, Christopher D Manning, and Curtis P Langlotz. Contrastive learning of medical visual representations from paired images and text. In *Machine Learning for Healthcare Conference*, pages 2–25. PMLR, 2022.
- [7] Hong-Yu Zhou, Chenyu Lian, Liansheng Wang, and Yizhou Yu. Advancing radiograph representation learning with masked record modeling. In *The Eleventh International Conference on Learning Representations*, 2023.
- [8] Chunyuan Li, Cliff Wong, Sheng Zhang, Naoto Usuyama, Haotian Liu, Jianwei Yang, Tristan Naumann, Hoifung Poon, and Jianfeng Gao. Llava-med: Training a large language-and-vision assistant for biomedicine in one day. *arXiv preprint arXiv:2306.00890*, 2023. URL <https://arxiv.org/pdf/2306.00890.pdf>.
- [9] Michael Moor, Qian Huang, Shirley Wu, Michihiro Yasunaga, Cyril Zakka, Yash Dalmia, Eduardo Pontes Reis, Pranav Rajpurkar, and Jure Leskovec. Med-flamingo: a multimodal medical few-shot learner. *arXiv preprint arXiv:2307.15189*, 2023. URL <https://arxiv.org/pdf/2307.15189.pdf>.

- [10] Tao Tu, Shekoofeh Azizi, Danny Driess, Mike Schaeckermann, Mohamed Amin, Pi-Chuan Chang, Andrew Carroll, Chuck Lau, Ryutaro Tanno, Ira Ktena, et al. Towards generalist biomedical ai. *arXiv preprint arXiv:2307.14334*, 2023. URL <https://arxiv.org/pdf/2307.14334.pdf>.
- [11] Michael Moor, Oishi Banerjee, Zahra Shakeri Hossein Abad, Harlan M Krumholz, Jure Leskovec, Eric J Topol, and Pranav Rajpurkar. Foundation models for generalist medical artificial intelligence. *Nature*, 616(7956):259–265, 2023.
- [12] Mostafa Dehghani, Josip Djolonga, Basil Mustafa, Piotr Padlewski, Jonathan Heek, Justin Gilmer, Andreas Peter Steiner, Mathilde Caron, Robert Geirhos, Ibrahim Alabdulmohsin, et al. Scaling vision transformers to 22 billion parameters. In *International Conference on Machine Learning*, pages 7480–7512. PMLR, 2023.
- [13] Xiaohua Zhai, Alexander Kolesnikov, Neil Houlsby, and Lucas Beyer. Scaling vision transformers. In *Proceedings of the IEEE/CVF Conference on Computer Vision and Pattern Recognition*, pages 12104–12113, 2022.
- [14] Jinyu Yang, Jiali Duan, Son Tran, Yi Xu, Sampath Chanda, Liqun Chen, Belinda Zeng, Trishul Chilimbi, and Junzhou Huang. Vision-language pre-training with triple contrastive learning. In *Proceedings of the IEEE/CVF Conference on Computer Vision and Pattern Recognition*, pages 15671–15680, 2022.
- [15] Xiaohua Zhai, Xiao Wang, Basil Mustafa, Andreas Steiner, Daniel Keysers, Alexander Kolesnikov, and Lucas Beyer. Lit: Zero-shot transfer with locked-image text tuning. In *Proceedings of the IEEE/CVF Conference on Computer Vision and Pattern Recognition*, pages 18123–18133, 2022.
- [16] Victor Weixin Liang, Yuhui Zhang, Yongchan Kwon, Serena Yeung, and James Y Zou. Mind the gap: Understanding the modality gap in multi-modal contrastive representation learning. *Advances in Neural Information Processing Systems*, 35:17612–17625, 2022.
- [17] Alistair EW Johnson, Tom J Pollard, Seth J Berkowitz, Nathaniel R Greenbaum, Matthew P Lungren, Chih-ying Deng, Roger G Mark, and Steven Horng. MIMIC-CXR, a de-identified publicly available database of chest radiographs with free-text reports. *Scientific data*, 6(1):317, 2019. URL <https://physionet.org/content/mimic-cxr/2.0.0/>.
- [18] Aaron van den Oord, Yazhe Li, and Oriol Vinyals. Representation learning with contrastive predictive coding. *arXiv preprint arXiv:1807.03748*, 2018. URL <https://arxiv.org/pdf/1807.03748.pdf>.
- [19] Ting Chen, Simon Kornblith, Mohammad Norouzi, and Geoffrey Hinton. A simple framework for contrastive learning of visual representations. In *International conference on machine learning*, pages 1597–1607. PMLR, 2020. URL <https://proceedings.mlr.press/v119/chen20j/chen20j.pdf>.
- [20] Julián N Acosta, Guido J Falcone, Pranav Rajpurkar, and Eric J Topol. Multimodal biomedical ai. *Nature Medicine*, 28(9):1773–1784, 2022.
- [21] Curtis P Langlotz. The future of ai and informatics in radiology: 10 predictions, 2023.
- [22] Maxime Oquab, Timothée Darcret, Théo Moutakanni, Huy V. Vo, Marc Szafraniec, Vasil Khalidov, Pierre Fernandez, Daniel HAZIZA, Francisco Massa, Alaaeldin El-Nouby, Mido Assran, Nicolas Ballas, Wojciech Galuba, Russell Howes, Po-Yao Huang, Shang-Wen Li, Ishan Misra, Michael Rabbat, Vasu Sharma, Gabriel Synnaeve, Hu Xu, Herve Jegou, Julien Mairal, Patrick Labatut, Armand Joulin, and Piotr Bojanowski. DINov2: Learning robust visual features without supervision. *Transactions on Machine Learning Research*, 2024. ISSN 2835-8856. URL <https://openreview.net/forum?id=a68SUt6zFt>.
- [23] Zhicheng Huang, Xiaojie Jin, Chengze Lu, Qibin Hou, Ming-Ming Cheng, Dongmei Fu, Xiaohui Shen, and Jiashi Feng. Contrastive masked autoencoders are stronger vision learners. *IEEE Transactions on Pattern Analysis and Machine Intelligence*, 2023.
- [24] Namuk Park, Wonjae Kim, Byeongho Heo, Taekyung Kim, and Sangdoo Yun. What do self-supervised vision transformers learn? In *The Eleventh International Conference on Learning Representations*, 2023.
- [25] Shashank Shekhar, Florian Bordes, Pascal Vincent, and Ari S Morcos. Objectives matter: Understanding the impact of self-supervised objectives on vision transformer representations. In *ICLR 2023 Workshop on Mathematical and Empirical Understanding of Foundation Models*, 2023.

- [26] Olaf Ronneberger, Philipp Fischer, and Thomas Brox. U-net: Convolutional networks for biomedical image segmentation. In *Medical Image Computing and Computer-Assisted Intervention–MICCAI 2015: 18th International Conference, Munich, Germany, October 5–9, 2015, Proceedings, Part III 18*, pages 234–241. Springer, 2015.
- [27] Ze Liu, Yutong Lin, Yue Cao, Han Hu, Yixuan Wei, Zheng Zhang, Stephen Lin, and Baining Guo. Swin transformer: Hierarchical vision transformer using shifted windows. In *Proceedings of the IEEE/CVF international conference on computer vision*, pages 10012–10022, 2021.
- [28] Yanghao Li, Hanzi Mao, Ross Girshick, and Kaiming He. Exploring plain vision transformer backbones for object detection. In *European Conference on Computer Vision*, pages 280–296. Springer, 2022.
- [29] Tete Xiao, Yingcheng Liu, Bolei Zhou, Yunling Jiang, and Jian Sun. Unified perceptual parsing for scene understanding. In *Proceedings of the European conference on computer vision (ECCV)*, pages 418–434, 2018. URL https://openaccess.thecvf.com/content_ECCV_2018/papers/Tete_Xiao_Unified_Perceptual_Parsing_ECCV_2018_paper.pdf.
- [30] Zongwei Zhou, Vatsal Sodha, Md Mahfuzur Rahman Siddiquee, Ruibin Feng, Nima Tajbakhsh, Michael B Gotway, and Jianming Liang. Models genesis: Generic autodidactic models for 3d medical image analysis. In *Medical Image Computing and Computer Assisted Intervention–MICCAI 2019: 22nd International Conference, Shenzhen, China, October 13–17, 2019, Proceedings, Part IV 22*, pages 384–393. Springer, 2019.
- [31] Yucheng Tang, Dong Yang, Wenqi Li, Holger R Roth, Bennett Landman, Daguang Xu, Vishwesh Nath, and Ali Hatamizadeh. Self-supervised pre-training of swin transformers for 3d medical image analysis. In *Proceedings of the IEEE/CVF Conference on Computer Vision and Pattern Recognition*, pages 20730–20740, 2022.
- [32] Mahmoud Assran, Quentin Duval, Ishan Misra, Piotr Bojanowski, Pascal Vincent, Michael Rabbat, Yann LeCun, and Nicolas Ballas. Self-supervised learning from images with a joint-embedding predictive architecture. In *Proceedings of the IEEE/CVF Conference on Computer Vision and Pattern Recognition*, pages 15619–15629, 2023.
- [33] Mathilde Caron, Hugo Touvron, Ishan Misra, Hervé Jégou, Julien Mairal, Piotr Bojanowski, and Armand Joulin. Emerging properties in self-supervised vision transformers. In *Proceedings of the IEEE/CVF international conference on computer vision*, pages 9650–9660, 2021.
- [34] Jinghao Zhou, Chen Wei, Huiyu Wang, Wei Shen, Cihang Xie, Alan Yuille, and Tao Kong. iBOT: image BERT pre-training with online tokenizer. In *International Conference on Learning Representations*, 2022.
- [35] Ha Q Nguyen, Khanh Lam, Linh T Le, Hieu H Pham, Dat Q Tran, Dung B Nguyen, Dung D Le, Chi M Pham, Hang TT Tong, Diep H Dinh, et al. Vindr-cxr: An open dataset of chest x-rays with radiologist’s annotations. *Scientific Data*, 9(1):429, 2022.
- [36] Shruthi Bannur, Stephanie Hyland, Qianchu Liu, Fernando Perez-Garcia, Maximilian Ilse, Daniel C Castro, Benedikt Boecking, Harshita Sharma, Kenza Bouzid, Anja Thieme, et al. Learning to exploit temporal structure for biomedical vision-language processing. In *Proceedings of the IEEE/CVF Conference on Computer Vision and Pattern Recognition*, pages 15016–15027, 2023.
- [37] Sheng Zhang, Yanbo Xu, Naoto Usuyama, Jaspreet Bagga, Robert Tinn, Sam Preston, Rajesh Rao, Mu Wei, Naveen Valluri, Cliff Wong, et al. Large-scale domain-specific pretraining for biomedical vision-language processing. *arXiv preprint arXiv:2303.00915*, 2023. URL <https://arxiv.org/pdf/2303.00915.pdf>.
- [38] Ekin Tiu, Ellie Talius, Pujan Patel, Curtis P Langlotz, Andrew Y Ng, and Pranav Rajpurkar. Expert-level detection of pathologies from unannotated chest x-ray images via self-supervised learning. *Nature Biomedical Engineering*, 6(12):1399–1406, 2022.
- [39] Sijing Feng, Damian Azzollini, Ji Soo Kim, Cheng-Kai Jin, Simon P Gordon, Jason Yeoh, Eve Kim, Mina Han, Andrew Lee, Aakash Patel, et al. Curation of the candid-ptx dataset with free-text reports. *Radiology: Artificial Intelligence*, 3(6):e210136, 2021.
- [40] Anouk Stein MD, Carol Wu, Chris Carr, George Shih, Jamie Dulkowski, kalpathy, Leon Chen, Luciano Prevedello, Marc Kohli MD, Mark McDonald, Peter, Phil Culliton, Safwan Halabi MD, and Tian Xia. Rsna pneumonia detection challenge, 2018. URL <https://kaggle.com/competitions/rsna-pneumonia-detection-challenge>.

- [41] Zhenda Xie, Zheng Zhang, Yue Cao, Yutong Lin, Yixuan Wei, Qi Dai, and Han Hu. On data scaling in masked image modeling. In *Proceedings of the IEEE/CVF Conference on Computer Vision and Pattern Recognition*, pages 10365–10374, 2023.
- [42] Mehdi Cherti and Jenia Jitsev. Effect of pre-training scale on intra-and inter-domain, full and few-shot transfer learning for natural and x-ray chest images. In *2022 International Joint Conference on Neural Networks (IJCNN)*, pages 1–9. IEEE, 2022. URL <https://arxiv.org/pdf/2106.00116.pdf>.
- [43] Basil Mustafa, Aaron Loh, Jan Freyberg, Patricia MacWilliams, Megan Wilson, Scott Mayer McKinney, Marcin Sieniek, Jim Winkens, Yuan Liu, Peggy Bui, et al. Supervised transfer learning at scale for medical imaging. *arXiv preprint arXiv:2101.05913*, 2021. URL <https://arxiv.org/pdf/2101.05913.pdf>.
- [44] Hadrien Bertrand, Mohammad Hashir, and Joseph Paul Cohen. Do lateral views help automated chest x-ray predictions? *arXiv preprint arXiv:1904.08534*, 2019. URL <https://arxiv.org/pdf/1904.08534.pdf>.
- [45] Mohammad Hashir, Hadrien Bertrand, and Joseph Paul Cohen. Quantifying the value of lateral views in deep learning for chest x-rays. In *Medical Imaging with Deep Learning*, pages 288–303. PMLR, 2020. URL <https://proceedings.mlr.press/v121/hashir20a/hashir20a.pdf>.
- [46] Mathilde Caron, Ishan Misra, Julien Mairal, Priya Goyal, Piotr Bojanowski, and Armand Joulin. Unsupervised learning of visual features by contrasting cluster assignments. *Advances in neural information processing systems*, 33:9912–9924, 2020.
- [47] Dina Demner-Fushman, Marc D Kohli, Marc B Rosenman, Sonya E Shooshan, Laritza Rodriguez, Sameer Antani, George R Thoma, and Clement J McDonald. Preparing a collection of radiology examinations for distribution and retrieval. *Journal of the American Medical Informatics Association*, 23(2):304–310, 2016.
- [48] Haotian Liu, Chunyuan Li, Qingyang Wu, and Yong Jae Lee. Visual instruction tuning, 2023. URL <http://arxiv.org/abs/2304.08485>.
- [49] Haotian Liu, Chunyuan Li, Yuheng Li, and Yong Jae Lee. Improved baselines with visual instruction tuning, 2023. URL <http://arxiv.org/pdf/2310.03744.pdf>.
- [50] Wei-Lin Chiang, Zhuohan Li, Zi Lin, Ying Sheng, Zhanghao Wu, Hao Zhang, Lianmin Zheng, Siyuan Zhuang, Yonghao Zhuang, Joseph E. Gonzalez, Ion Stoica, and Eric P. Xing. Vicuna: An open-source chatbot impressing gpt-4 with 90%* chatgpt quality, March 2023. URL <https://lmsys.org/blog/2023-03-30-vicuna/>.
- [51] Ziyu Yang, Santhosh Cherian, and Slobodan Vucetic. Data augmentation for radiology report simplification. In *Findings of the Association for Computational Linguistics: EACL 2023*, pages 1877–1887, 2023.
- [52] Chin-Yew Lin. ROUGE: A package for automatic evaluation of summaries. In *Text Summarization Branches Out*, pages 74–81. Association for Computational Linguistics, July 2004. URL <https://aclanthology.org/W04-1013>.
- [53] Kishore Papineni, Salim Roukos, Todd Ward, and Wei-Jing Zhu. BLEU: a method for automatic evaluation of machine translation. In *Proceedings of the 40th Annual Meeting of the Association for Computational Linguistics*, pages 311–318. Association for Computational Linguistics, July 2002. doi:[10.3115/1073083.1073135](https://doi.org/10.3115/1073083.1073135).
- [54] Jean-Benoit Delbrouck, Pierre Chambon, Christian Blethgen, Emily Tsai, Omar Almusa, and Curtis Langlotz. Improving the factual correctness of radiology report generation with semantic rewards. In *Findings of the Association for Computational Linguistics: EMNLP 2022*, pages 4348–4360. ACL, December 2022. doi:[10.18653/v1/2022.findings-emnlp.319](https://doi.org/10.18653/v1/2022.findings-emnlp.319).
- [55] Akshay Smit, Saahil Jain, Pranav Rajpurkar, Anuj Pareek, Andrew Ng, and Matthew Lungren. Combining automatic labelers and expert annotations for accurate radiology report labeling using BERT. In *Proceedings of the 2020 Conference on Empirical Methods in Natural Language Processing (EMNLP)*, pages 1500–1519. ACL, November 2020. doi:[10.18653/v1/2020.emnlp-main.117](https://doi.org/10.18653/v1/2020.emnlp-main.117).
- [56] Jeremy Irvin, Pranav Rajpurkar, Michael Ko, Yifan Yu, Silvana Ciurea-Ilcus, Chris Chute, Henrik Marklund, Behzad Haghgoo, Robyn L. Ball, Katie Shpanskaya, Jayne Seekins, David A. Mong, Safwan S. Halabi, Jesse K. Sandberg, Ricky Jones, David B. Larson, Curtis P. Langlotz, Bhavik N. Patel, Matthew P. Lungren, and Andrew Y. Ng. CheXpert: A large chest radiograph dataset with uncertainty labels and expert comparison. In *Proceedings of the AAAI Conference on Artificial Intelligence (AAAI 2019)*, volume 33, pages 590–597. AAAI Press, July 2019. doi:[10.1609/aaai.v33i01.3301590](https://doi.org/10.1609/aaai.v33i01.3301590).

- [57] Ji Lin, Hongxu Yin, Wei Ping, Yao Lu, Pavlo Molchanov, Andrew Tao, Huizi Mao, Jan Kautz, Mohammad Shoeybi, and Song Han. Vila: On pre-training for visual language models. *arXiv preprint arXiv:2312.07533*, 2023. URL <https://arxiv.org/pdf/2312.07533.pdf>.
- [58] Tsung-Yi Lin, Piotr Dollár, Ross Girshick, Kaiming He, Bharath Hariharan, and Serge Belongie. Feature pyramid networks for object detection. In *Proceedings of the IEEE conference on computer vision and pattern recognition*, pages 2117–2125, 2017.
- [59] Reza Azad, Ehsan Khodapanah Aghdam, Amelie Rauland, Yiwei Jia, Atlas Haddadi Avval, Afshin Bozorgpour, Sanaz Karimijafarbigloo, Joseph Paul Cohen, Ehsan Adeli, and Dorit Merhof. Medical image segmentation review: The success of u-net, 2022.
- [60] Fabian Isensee, Jens Petersen, Andre Klein, David Zimmerer, Paul F. Jaeger, Simon Kohl, Jakob Wasserthal, Gregor Koehler, Tobias Norajitra, Sebastian Wirkert, and Klaus H. Maier-Hein. nnu-net: Self-adapting framework for u-net-based medical image segmentation. *arXiv preprint arXiv:1809.10486*, 2018. URL <https://arxiv.org/pdf/1809.10486.pdf>.
- [61] Mingxing Tan and Quoc V. Le. Efficientnet: Rethinking model scaling for convolutional neural networks. *arXiv preprint arXiv:1905.11946*, 2020. URL <https://arxiv.org/pdf/1905.11946.pdf>.
- [62] Gabriel Ilharco, Mitchell Wortsman, Ross Wightman, Cade Gordon, Nicholas Carlini, Rohan Taori, Achal Dave, Vaishaal Shankar, Hongseok Namkoong, John Miller, Hannaneh Hajishirzi, Ali Farhadi, and Ludwig Schmidt. OpenCLIP, September 2022. URL <https://doi.org/10.5281/zenodo.7086307>.
- [63] Joy T Wu, Nkechinyere N Agu, Ismini Lourentzou, Arjun Sharma, Joseph A Paguio, Jasper S Yao, Edward C Dee, William Mitchell, Satyananda Kashyap, Andrea Giovannini, et al. Chest imangenome dataset (version 1.0). *PhysioNet*, 5:18, 2021.
- [64] Hongyu Wang, Dandan Zhang, Jun Feng, Lucia Cascone, Michele Nappi, and Shaohua Wan. A multi-objective segmentation method for chest x-rays based on collaborative learning from multiple partially annotated datasets. *Information Fusion*, 102:102016, 2024.
- [65] Dandan Zhang, Hongyu Wang, Jiahui Deng, Tonghui Wang, Cong Shen, and Jun Feng. Cams-net: An attention-guided feature selection network for rib segmentation in chest x-rays. *Computers in Biology and Medicine*, 156:106702, 2023.
- [66] Debojyoti Pal, Tanushree Meena, and Sudipta Roy. A fully connected reproducible se-uresnet for multiorgan chest radiographs segmentation. In *2023 IEEE 24th International Conference on Information Reuse and Integration for Data Science (IRI)*, pages 261–266. IEEE, 2023.
- [67] Ricardo Coimbra Briosso, João Pedrosa, Ana Maria Mendonça, and Aurélio Campilho. Semi-supervised multi-structure segmentation in chest x-ray imaging. In *2023 IEEE 36th International Symposium on Computer-Based Medical Systems (CBMS)*, pages 814–820. IEEE, 2023.
- [68] Jane Bromley, Isabelle Guyon, Yann LeCun, Eduard Säckinger, and Roopak Shah. Signature verification using a "siamese" time delay neural network. In J. Cowan, G. Tesauro, and J. Alspector, editors, *Advances in Neural Information Processing Systems*, volume 6. Morgan-Kaufmann, 1993. URL https://proceedings.neurips.cc/paper_files/paper/1993/file/288cc0ff022877bd3df94bc9360b9c5d-Paper.pdf.
- [69] Antti Tarvainen and Harri Valpola. Mean teachers are better role models: Weight-averaged consistency targets improve semi-supervised deep learning results. *Advances in neural information processing systems*, 30, 2017.
- [70] Hangbo Bao, Li Dong, Songhao Piao, and Furu Wei. Beit: Bert pre-training of image transformers. In *International Conference on Learning Representations*, 2021.
- [71] Xiao Wang, Haoqi Fan, Yuandong Tian, Daisuke Kihara, and Xinlei Chen. On the importance of asymmetry for siamese representation learning. In *Proceedings of the IEEE/CVF Conference on Computer Vision and Pattern Recognition*, pages 16570–16579, 2022.
- [72] Alexandre Sablayrolles, Matthijs Douze, Cordelia Schmid, and Hervé Jégou. Spreading vectors for similarity search. In *International Conference on Learning Representations*, 2018.
- [73] Sangjoon Park, Gwanghyun Kim, Yujin Oh, Joon Beom Seo, Sang Min Lee, Jin Hwan Kim, Sungjun Moon, Jae-Kwang Lim, Chang Min Park, and Jong Chul Ye. Self-evolving vision transformer for chest x-ray diagnosis through knowledge distillation. *Nature communications*, 13(1):3848, 2022.

- [74] Adrien Bardes, Jean Ponce, and Yann LeCun. Vicregl: Self-supervised learning of local visual features. *Advances in Neural Information Processing Systems*, 35:8799–8810, 2022.
- [75] Li-Ching Chen, Po-Chih Kuo, Ryan Wang, Judy Gichoya, and Leo Anthony Celi. Chest x-ray segmentation images based on mimic-cxr, 2022. URL <https://physionet.org/content/lung-segment-mimic-cxr/1.0.0/>.
- [76] Hoang C. Nguyen, Tung T. Le, Hieu H. Pham, and Ha Q. Nguyen. Vindr-ribcxr: A benchmark dataset for automatic segmentation and labeling of individual ribs on chest x-rays, 2021.
- [77] Johannes Boos, Rotem S Lanzman, Philipp Heusch, Joel Aissa, Christoph Schleich, Christoph Thomas, Lino M Sawicki, Gerald Antoch, and Patric Kröpil. Does body mass index outperform body weight as a surrogate parameter in the calculation of size-specific dose estimates in adult body ct? *The British Journal of Radiology*, 89(1059):20150734, 2016.
- [78] Aydin Demircioğlu, Anton S Quinsten, Lale Umutlu, Michael Forsting, Kai Nassenstein, and Denise Bos. Determining body height and weight from thoracic and abdominal ct localizers in pediatric and young adult patients using deep learning. *Scientific Reports*, 13(1):19010, 2023.
- [79] Shota Ichikawa, Misaki Hamada, and Hiroyuki Sugimori. A deep-learning method using computed tomography scout images for estimating patient body weight. *Scientific reports*, 11(1):15627, 2021.
- [80] Alistair Johnson, Lucas Bulgarelli, Tom Pollard, Steven Horng, Leo Anthony Celi, and Roger Mark. Mimic-iv, 2023. URL <https://physionet.org/content/mimiciv/2.2/>.
- [81] Joana Palés Huix, Adithya Raju Ganeshan, Johan Fredin Haslum, Magnus Söderberg, Christos Matsoukas, and Kevin Smith. Are natural domain foundation models useful for medical image classification? In *Proceedings of the IEEE/CVF Winter Conference on Applications of Computer Vision*, pages 7634–7643, 2024.
- [82] Zhongwei Wan, Che Liu, Mi Zhang, Jie Fu, Benyou Wang, Sibo Cheng, Lei Ma, Cesar C’esar Quilodr’an-Casas, and Rossella Arcucci. Med-unic: Unifying cross-lingual medical vision-language pre-training by diminishing bias. *Advances in Neural Information Processing Systems*, 2023.
- [83] Tom Brown, Benjamin Mann, Nick Ryder, Melanie Subbiah, Jared D Kaplan, Prafulla Dhariwal, Arvind Neelakantan, Pranav Shyam, Girish Sastry, Amanda Askell, et al. Language models are few-shot learners. *Advances in neural information processing systems*, 33:1877–1901, 2020.
- [84] Josh Achiam, Steven Adler, Sandhini Agarwal, Lama Ahmad, Ilge Akkaya, Florencia Leoni Aleman, Diogo Almeida, Janko Altenschmidt, Sam Altman, Shyamal Anadkat, et al. Gpt-4 technical report. *arXiv preprint arXiv:2303.08774*, 2023. URL <https://arxiv.org/pdf/2303.08774.pdf>.
- [85] Harsha Nori, Yin Tat Lee, Sheng Zhang, Dean Carignan, Richard Edgar, Nicolo Fusi, Nicholas King, Jonathan Larson, Yuanzhi Li, Weishung Liu, et al. Can generalist foundation models outcompete special-purpose tuning? case study in medicine. *arXiv preprint arXiv:2311.16452*, 2023. URL <https://arxiv.org/pdf/2311.16452.pdf>.
- [86] Dongsheng Jiang, Yuchen Liu, Songlin Liu, Xiaopeng Zhang, Jin Li, Hongkai Xiong, and Qi Tian. From clip to dino: Visual encoders shout in multi-modal large language models, 2023. URL <https://arxiv.org/pdf/2310.08825v1.pdf>.
- [87] Xiaosong Wang, Yifan Peng, Le Lu, Zhiyong Lu, Mohammadadi Bagheri, and Ronald M Summers. Chestx-ray8: Hospital-scale chest x-ray database and benchmarks on weakly-supervised classification and localization of common thorax diseases. In *Proceedings of the IEEE conference on computer vision and pattern recognition*, pages 2097–2106, 2017.
- [88] Aurelia Bustos, Antonio Pertusa, Jose-Maria Salinas, and Maria de la Iglesia-Vayá. PadChest: A large chest x-ray image dataset with multi-label annotated reports. *Medical Image Analysis*, 66:101797, December 2020. ISSN 1361-8415. doi:[10.1016/j.media.2020.101797](https://doi.org/10.1016/j.media.2020.101797). URL <http://dx.doi.org/10.1016/j.media.2020.101797>.
- [89] Ary L. Goldberger, Luis A. N. Amaral, Leon Glass, Jeffrey M. Hausdorff, Plamen Ch. Ivanov, Roger G. Mark, Joseph E. Mietus, George B. Moody, Chung-Kang Peng, and H. Eugene Stanley. Physiobank, physiotoolkit, and physionet. *Circulation*, 101(23):e215–e220, 2000. doi:[10.1161/01.CIR.101.23.e215](https://doi.org/10.1161/01.CIR.101.23.e215). URL <https://www.ahajournals.org/doi/abs/10.1161/01.CIR.101.23.e215>.

- [90] Eduardo P Reis, Joselisa PQ de Paiva, Maria CB da Silva, Guilherme AS Ribeiro, Victor F Paiva, Lucas Bulgarelli, Henrique MH Lee, Paulo V Santos, Vanessa M Brito, Lucas TW Amaral, et al. BRAX, Brazilian labeled chest x-ray dataset. *Scientific Data*, 9(1):487, 2022.
- [91] Jean-Bastien Grill, Florian Strub, Florent Altché, Corentin Tallec, Pierre Richemond, Elena Buchatskaya, Carl Doersch, Bernardo Avila Pires, Zhaohan Guo, Mohammad Gheshlaghi Azar, et al. Bootstrap your own latent-a new approach to self-supervised learning. *Advances in neural information processing systems*, 33:21271–21284, 2020.
- [92] Xinlei Chen and Kaiming He. Exploring simple siamese representation learning. In *Proceedings of the IEEE/CVF conference on computer vision and pattern recognition*, pages 15750–15758, 2021.
- [93] Kaiming He, Xinlei Chen, Saining Xie, Yanghao Li, Piotr Dollár, and Ross Girshick. Masked autoencoders are scalable vision learners. In *Proceedings of the IEEE/CVF conference on computer vision and pattern recognition*, pages 16000–16009, 2022.
- [94] Sheng Shen, Chunyuan Li, Xiaowei Hu, Yujia Xie, Jianwei Yang, Pengchuan Zhang, Zhe Gan, Lijuan Wang, Lu Yuan, Ce Liu, et al. K-lite: Learning transferable visual models with external knowledge. *Advances in Neural Information Processing Systems*, 35:15558–15573, 2022.
- [95] Lewei Yao, Runhui Huang, Lu Hou, Guansong Lu, Minzhe Niu, Hang Xu, Xiaodan Liang, Zhengu Li, Xin Jiang, and Chunjing Xu. Filip: Fine-grained interactive language-image pre-training. In *International Conference on Learning Representations*, 2021.
- [96] Rohit Girdhar, Alaaeldin El-Nouby, Zhuang Liu, Mannat Singh, Kalyan Vasudev Alwala, Armand Joulin, and Ishan Misra. Imagebind: One embedding space to bind them all. In *Proceedings of the IEEE/CVF Conference on Computer Vision and Pattern Recognition*, pages 15180–15190, 2023.
- [97] Jiahui Yu, Zirui Wang, Vijay Vasudevan, Legg Yeung, Mojtaba Seyedhosseini, and Yonghui Wu. Coca: Contrastive captioners are image-text foundation models. *Transactions on Machine Learning Research*, 2022. ISSN 2835-8856.
- [98] Zirui Wang, Jiahui Yu, Adams Wei Yu, Zihang Dai, Yulia Tsvetkov, and Yuan Cao. SimVLM: Simple visual language model pretraining with weak supervision. In *International Conference on Learning Representations*, 2022.
- [99] Amanpreet Singh, Ronghang Hu, Vedanuj Goswami, Guillaume Couairon, Wojciech Galuba, Marcus Rohrbach, and Douwe Kiela. Flava: A foundational language and vision alignment model. In *Proceedings of the IEEE/CVF Conference on Computer Vision and Pattern Recognition*, pages 15638–15650, 2022.
- [100] Michael Tschanne, Manoj Kumar, Andreas Steiner, Xiaohua Zhai, Neil Houlsby, and Lucas Beyer. Image captioners are scalable vision learners too. *arXiv preprint arXiv:2306.07915*, 2023. URL <https://arxiv.org/pdf/2306.07915.pdf>.
- [101] Yangguang Li, Feng Liang, Lichen Zhao, Yufeng Cui, Wanli Ouyang, Jing Shao, Fengwei Yu, and Junjie Yan. Supervision exists everywhere: A data efficient contrastive language-image pre-training paradigm. In *International Conference on Learning Representations*, 2021.
- [102] Floris Weers, Vaishaal Shankar, Angelos Katharopoulos, Yinfei Yang, and Tom Gunter. Masked autoencoding does not help natural language supervision at scale. In *Proceedings of the IEEE/CVF Conference on Computer Vision and Pattern Recognition*, pages 23432–23444, 2023.
- [103] Norman Mu, Alexander Kirillov, David Wagner, and Saining Xie. Slip: Self-supervision meets language-image pre-training. In *European Conference on Computer Vision*, pages 529–544. Springer, 2022.
- [104] Chaoyi Wu, Xiaoman Zhang, Ya Zhang, Yanfeng Wang, and Weidi Xie. Medklip: Medical knowledge enhanced language-image pre-training for x-ray diagnosis. In *Proceedings of the IEEE/CVF International Conference on Computer Vision (ICCV)*, pages 21372–21383, October 2023. URL https://openaccess.thecvf.com/content/ICCV2023/papers/Wu_MedKLIP_Medical_Knowledge_Enhanced_Language-Image_Pre-Training_for_X-ray_Diagnosis_ICCV_2023_paper.pdf.
- [105] Weixiong Lin, Ziheng Zhao, Xiaoman Zhang, Chaoyi Wu, Ya Zhang, Yanfeng Wang, and Weidi Xie. Pmc-clip: Contrastive language-image pre-training using biomedical documents. *arXiv preprint arXiv:2303.07240*, 2023. URL <https://arxiv.org/pdf/2303.07240.pdf>.

- [106] Zifeng Wang, Zhenbang Wu, Dinesh Agarwal, and Jimeng Sun. Medclip: Contrastive learning from unpaired medical images and text, 2022. URL <https://arxiv.org/pdf/2210.10163.pdf>.
- [107] Jean-Baptiste Alayrac, Jeff Donahue, Pauline Luc, Antoine Miech, Iain Barr, Yana Hasson, Karel Lenc, Arthur Mensch, Katherine Millican, Malcolm Reynolds, et al. Flamingo: a visual language model for few-shot learning. *Advances in Neural Information Processing Systems*, 35:23716–23736, 2022.
- [108] Shekoofeh Azizi, Basil Mustafa, Fiona Ryan, Zachary Beaver, Jan Freyberg, Jonathan Deaton, Aaron Loh, Alan Karthikesalingam, Simon Kornblith, Ting Chen, et al. Big self-supervised models advance medical image classification. In *Proceedings of the IEEE/CVF international conference on computer vision*, pages 3478–3488, 2021.
- [109] Shekoofeh Azizi, Laura Culp, Jan Freyberg, Basil Mustafa, Sebastien Baur, Simon Kornblith, Ting Chen, Nenad Tomasev, Jovana Mitrović, Patricia Strachan, et al. Robust and data-efficient generalization of self-supervised machine learning for diagnostic imaging. *Nature Biomedical Engineering*, pages 1–24, 2023.
- [110] Zekai Chen, Devansh Agarwal, Kshitij Aggarwal, Wiem Safta, Mariann Micsinai Balan, and Kevin Brown. Masked image modeling advances 3d medical image analysis. In *Proceedings of the IEEE/CVF Winter Conference on Applications of Computer Vision*, pages 1970–1980, 2023.
- [111] Zhenda Xie, Zheng Zhang, Yue Cao, Yutong Lin, Jianmin Bao, Zhuliang Yao, Qi Dai, and Han Hu. Simmim: A simple framework for masked image modeling. In *Proceedings of the IEEE/CVF Conference on Computer Vision and Pattern Recognition*, pages 9653–9663, 2022.
- [112] Mohammad Reza Hosseinzadeh Taher, Michael B Gotway, and Jianming Liang. Towards foundation models learned from anatomy in medical imaging via self-supervision. In *MICCAI Workshop on Domain Adaptation and Representation Transfer*, pages 94–104. Springer, 2023.
- [113] Alexandre Filiot, Ridouane Ghermi, Antoine Olivier, Paul Jacob, Lucas Fidon, Alice Mac Kain, Charlie Saillard, and Jean-Baptiste Schiratti. Scaling self-supervised learning for histopathology with masked image modeling. *medRxiv*, pages 2023–07, 2023. URL <https://www.medrxiv.org/content/10.1101/2023.07.21.23292757v2.full.pdf>.
- [114] Eugene Vorontsov, Alican Bozkurt, Adam Casson, George Shaikovski, Michal Zelechowski, Siqi Liu, Philippe Mathieu, Alexander van Eck, Donghun Lee, Julian Viret, Eric Robert, Yi Kan Wang, Jeremy D. Kunz, Matthew C. H. Lee, Jan Bernhard, Ran A. Godrich, Gerard Oakley, Ewan Millar, Matthew Hanna, Juan Retamero, William A. Moye, Razik Yousfi, Christopher Kanan, David Klimstra, Brandon Rothrock, and Thomas J. Fuchs. Virchow: A million-slide digital pathology foundation model. *arXiv preprint arXiv:2309.07778*, 2023. URL <https://arxiv.org/pdf/2309.07778.pdf>.
- [115] Erdi Çallı, Ecem Sogancioglu, Bram van Ginneken, Kicky G van Leeuwen, and Keelin Murphy. Deep learning for chest x-ray analysis: A survey. *Medical Image Analysis*, 72:102125, 2021.
- [116] Andrew B Sellergren, Christina Chen, Zaid Nabulsi, Yuanzhen Li, Aaron Maschinot, Aaron Sarna, Jenny Huang, Charles Lau, Sreenivasa Raju Kalidindi, Mozziyar Etemadi, et al. Simplified transfer learning for chest radiography models using less data. *Radiology*, 305(2):454–465, 2022.
- [117] Luke Oakden-Rayner. Exploring large-scale public medical image datasets. *Academic radiology*, 27(1):106–112, 2020.
- [118] Anna Majkowska, Sid Mittal, David F Steiner, Joshua J Reicher, Scott Mayer McKinney, Gavin E Duggan, Krish Eswaran, Po-Hsuan Cameron Chen, Yun Liu, Sreenivasa Raju Kalidindi, et al. Chest radiograph interpretation with deep learning models: assessment with radiologist-adjudicated reference standards and population-adjusted evaluation. *Radiology*, 294(2):421–431, 2020.
- [119] Nicolás Gaggion, Candelaria Mosquera, Lucas Mansilla, Martina Aineseder, Diego H Milone, and Enzo Ferrante. Chexmask: a large-scale dataset of anatomical segmentation masks for multi-center chest x-ray images. *arXiv preprint arXiv:2307.03293*, 2023. URL <https://arxiv.org/pdf/2307.03293.pdf>.
- [120] Johannes Rueckel, Christian Huemmer, Andreas Fieselmann, Florin-Cristian Ghesu, Awais Mansoor, Balthasar Schachtnner, Philipp Wesp, Lena Trappmann, Basel Munawwar, Jens Ricke, et al. Pneumothorax detection in chest radiographs: optimizing artificial intelligence system for accuracy and confounding bias reduction using in-image annotations in algorithm training. *European radiology*, pages 1–13, 2021.

- [121] Mark Endo, Rayan Krishnan, Viswesh Krishna, Andrew Y Ng, and Pranav Rajpurkar. Retrieval-based chest x-ray report generation using a pre-trained contrastive language-image model. In *Machine Learning for Health*, pages 209–219. PMLR, 2021.
- [122] Yasuhide Miura, Yuhao Zhang, Emily Tsai, Curtis Langlotz, and Dan Jurafsky. Improving factual completeness and consistency of image-to-text radiology report generation. In *Proceedings of the 2021 Conference of the North American Chapter of the Association for Computational Linguistics: Human Language Technologies*, pages 5288–5304, 2021.
- [123] Md Inzamam Ul Haque, Abhishek K Dubey, Ioana Danciu, Amy C Justice, Olga S Ovchinnikova, and Jacob D Hinkle. Effect of image resolution on automated classification of chest x-rays. *Journal of Medical Imaging*, 10(4):044503–044503, 2023.
- [124] Carl F Sabottke and Bradley M Spieler. The effect of image resolution on deep learning in radiography. *Radiology: Artificial Intelligence*, 2(1):e190015, 2020.
- [125] Ryutaro Tanno, David GT Barrett, Andrew Sellergren, Sumedh Ghaisas, Sumanth Dathathri, Abigail See, Johannes Welbl, Karan Singhal, Shekoofeh Azizi, Tao Tu, et al. Consensus, dissensus and synergy between clinicians and specialist foundation models in radiology report generation. *arXiv preprint arXiv:2311.18260*, 2023. URL <https://arxiv.org/pdf/2311.18260.pdf>.
- [126] Grant Duffy, Shoa L. Clarke, Matthew Christensen, Bryan He, Neal Yuan, Susan Cheng, and David Ouyang. Confounders mediate AI prediction of demographics in medical imaging. *npj Digital Medicine*, 5(1):188, 2022. ISSN 2398-6352. doi:[10.1038/s41746-022-00720-8](https://doi.org/10.1038/s41746-022-00720-8). URL <https://www.nature.com/articles/s41746-022-00720-8>.
- [127] F. Pedregosa, G. Varoquaux, A. Gramfort, V. Michel, B. Thirion, O. Grisel, M. Blondel, P. Prettenhofer, R. Weiss, V. Dubourg, J. Vanderplas, A. Passos, D. Cournapeau, M. Brucher, M. Perrot, and E. Duchesnay. Scikit-learn: Machine learning in Python. *Journal of Machine Learning Research*, 12:2825–2830, 2011.

A Related work

A.1 Representation learning

Advances in representation learning come from a variety of directions, with recent approaches obtaining desired properties by combining methods. For image-only pre-training, contrastive objectives are powerful for learning useful global representations [19]; more recently, reliance on negative samples has been replaced with asymmetric architectures [91, 92] and clustering [46, 33]. For local feature learning, useful for tasks such as segmentation, generative tasks, namely masked image modelling has shown to be more useful [70, 93] and its data scaling characteristics studied in [41]. Such local MIM and global contrastive objectives can be combined effectively to capture features useful for more diverse tasks [34, 22, 23]. Recently [32] has shown that MIM-only learning coupled with advanced masking and latent-prediction strategies can improve the model convergence and reduce the reliance on multi-view contrastive objectives. Contrastive methods are similarly popular for image-text pre-training, mapping the two modalities to the same global feature space (CLIP; [2]), and have been shown to be effective for various downstream tasks. Proposals for improvements include using external knowledge bases [94], encouraging finer-level alignment [95], and binding multiple modalities [96]. Additional granularity in learned representations can be obtained via generative tasks such as captioning [97, 98, 99, 100]. Combining image-only objectives and image-text objectives has also been shown to be beneficial [15, 101, 102, 103].

A.2 Biomedical vision-language models

A number of other works have developed foundation models specialised for medical tasks. Many of these are based on multimodal contrastive learning [6], with ChexZero [38], GLoRIA [5], and BioViL [4] training solely on X-ray datasets, showing image- and patch-level variants of the CLIP objective. BioViL-T [36] introduces temporal knowledge into the learning process to make use of multiple X-rays and conditional reports. Med-UniC [82] has extended these approaches to multi-lingual datasets achieving superior performance. In [104], authors have introduced a joint space for multimodal samples by extracting clinical entity triplets from each modality and aligning them. A set of studies have focused on building new larger scale paired image-text datasets in order to match the scaling observed for natural image CLIP models: BiomedCLIP [37] build a larger dataset of image-text pairs by extracting figures from PubMed articles; PMC-CLIP [105] do similar, with additional data curation stages to filter for primarily X-ray images. MedCLIP [106] addresses medical data scarcity by decoupling image and text for multimodal contrastive learning, thus vastly scaling usable training data at a low cost. Similarly, masked-modelling has found its applications in this domain as well, achieving strong performance on various benchmarks [7]. Lastly, vision-language models have been developed based on generative captioning [97], with Med-Flamingo [9] fine-tuning a Flamingo [107] model on paired/interleaved image-text data.

A.3 Image-based self-supervised learning

Image-only pre-training for medical data has been extensively studied, with many recent works focusing on selecting pre-training objectives useful for the class of downstream applications of interest. For example, for classification, [73, 108, 109] demonstrated the use of SimCLR [19] and DINO-v.1 [33] contrastive approaches to learn transferable image features for downstream fine-tuning (also build more informative positive pairs); while for segmentation, Tang et al. [31] learn local features useful for CT and MR image segmentation by applying contrastive/predictive objectives to local regions, and [30, 110] use pixel-wise masked image modelling [93, 111] demonstrating strong performance across different imaging modalities. To learn features useful for medical tasks at multiple scales, Hosseinzadeh Taher et al. [112] decompose images in a coarse-to-fine manner and utilise contrastive predictive coding [18], while Zhou et al. [7] combine masked image modelling with masked language modelling, to learn a joint distribution and improve the fusion of modalities. Also of relevance are recent large-scale pre-trained image networks, specialised for the histopathology domain, which is notable for its abundant availability of imaging data; in similar research, authors in [113, 114] train iBoT [34] and DINOv2 [22] models respectively, arguing that contrastive methods are less suitable for rare pathologies since the linear separability of learned representations is poor for class-imbalanced data.

A.4 Applications of deep networks in radiology

A survey study [115] on chest X-Rays outlines various applications and benchmark datasets used in past studies. Sellergren et al. [116] have studied the transfer of pre-trained SSL features to classification tasks in reducing the requirement for manual labels. Similarly, early work [56, 87] explored the use of neural networks for image classification on large-scale datasets (ChestX-ray14 and CheXpert). In these benchmarks, diagnostic labels were extracted from radiology reports using a parser, resulting in significant label noise [117, 118]. Consequently, RAD-DINO and baselines

are evaluated only on benchmarks containing expert annotations. For medical image segmentation, in particular, U-Net [26] models remain widespread [59], whilst domain-specific approaches used priors tailored towards chest X-Rays [119]. Segmentation of findings have been also used to mitigate potential short-cuts and biases learnt by networks to disentangle abnormalities from treatment interventions [120]. Lastly, image backbones have been utilised for radiology report generation [10, 36, 121, 122] and VQA applications [8, 9] to extract visual descriptors that can be reasoned in conjunction with other clinical input data or textual prompts to generate text outputs.

B Ablation studies

Experimental analysis of different image networks can be confounded by factors such as image-resolution, training dataset and weight initialisation, which can lead to incomplete and sometimes misleading findings. Therefore, this study aims to first understand the impact of such factors on RAD-DINO and its benchmark results in isolation, before performing extensive evaluation against baseline biomedical models, taking these factors into account. In that regard, the following subsections present our learnings from ablations performed by running a multi-class linear classification on the VinDr-CXR dataset.

B.1 Dependence on image resolution

Image resolution has been shown to be an important factor in downstream prediction tasks [123, 124], and it can be a confounding factor on the performance gap between RAD-DINO and baseline image encoders that we observe in our experiments. In this section, we examine the impact of image resolution on large-scale or conspicuous findings (such as cardiomegaly and opacity), found in the VinDr-CXR [35] dataset, across the input resolution range of 224 to 518 pixels. Linear probing is performed, and AUPRC results are aggregated across findings in each dataset and multiple runs with different seeds. RAD-DINO is initialised from DINOv2 (ViT-B) for this ablation. Figure B.1 shows that for such large scale findings, the performance improvement of RAD-DINO is not necessarily attributed to its capability to encode higher resolution inputs—as long as input signal correlates with target objective, e.g. findings that manifest on large regions of the image. In contrast, in Appendix C.1, the same experiment is repeated for potentially small or subtle findings (including PTX and chest tubes), as found in the CANDID-PTX [39] dataset, where higher input resolution is required (see Figure C.1). In this scenario, we observe performance degradation as fine-granular details are lost, yet image-only learning still outperforms baseline approaches.

It is important to note that past research efforts on VQA [8, 9, 10] and text generation [10, 125], which leverage image backbones at lower resolutions, are likely hindered by the ambiguity of the input signal. This ambiguity may lead to hallucinations and performance limits, despite efforts to adapt large-scale text decoders with billions of model parameters on top of image embeddings.

B.2 Model weight initialisation

A series of ablations are carried out to inspect the role of pre-training on large-scale general domain datasets (e.g., LVD-142M) curated from over 1B images prior to in-domain training with chest X-ray images. Linear classification experiments are performed on the same VinDR benchmark by initialising the encoder parameters with random weights and ViT-B and comparing the large-scale DINO-v2 models (ViT-G and ViT-B) in the same setup. The results provided in Tables 1a and B.1 demonstrate that general-domain models transfer better to out-of-domain medical tasks with larger-scale architectures and training data, in particular compared to CLIP@336—and in some cases even better than small-scale backbones trained in-domain such as BioViL-T. This is in-line with the authors’ findings in [81, 42, 43]. However, continual pre-training with in-domain data leads to further gains (RAD-DINO), which plays more crucial role as initialisation from random weights consistently performs better than the backbones trained on general domain data. In particular, the general-domain pre-training contributes to better discrimination of findings that are less commonly seen in in-domain ICU medical datasets such as tuberculosis (TB) and pulmonary fibrosis (PF).

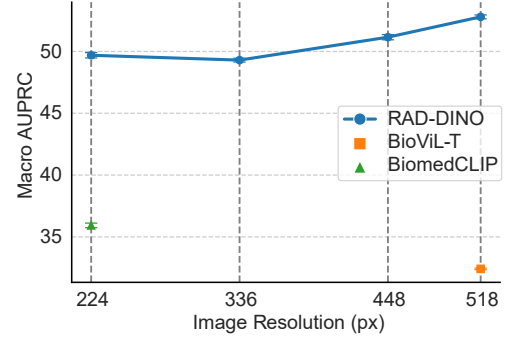


Figure B.1: Linear probing results on VinDr-CXR vs. input image resolution, where each given resolution is used for pre-training and inference. This demonstrates that, particularly for large-scale findings, the superior performance of RAD-DINO is not driven by its capability to encode higher resolution inputs. Data is presented as mean \pm standard deviation.

Table B.1: Linear classification results obtained on VinDr-CXR benchmark with 5-different seeds and training splits. Domain-transfer of large general-domain models is evaluated alongside continually pre-trained RAD-DINO network with DINOv2 (ViT-B) initialisation and in-domain data.

Model	LO	CM	PL-T	AE	PF	TB	PE	Agg
DINOv2 (ViT-B) [22]	11.6 ± 0.6	51.0 ± 0.7	27.5 ± 0.4	30.1 ± 0.3	28.4 ± 0.6	29.9 ± 1.2	42.5 ± 1.6	31.6
DINOv2 (ViT-G) [22]	13.0 ± 0.3	54.4 ± 0.4	25.1 ± 0.3	29.3 ± 0.2	30.1 ± 0.1	32.3 ± 0.5	50.1 ± 0.9	33.5
RAD-DINO (Random init.)	11.7 ± 0.2	73.7 ± 0.4	31.7 ± 0.8	41.1 ± 0.2	39.7 ± 0.6	46.7 ± 0.7	76.7 ± 0.3	45.9
RAD-DINO (Continual)	14.9 ± 0.2	69.9 ± 0.3	36.6 ± 0.6	44.6 ± 0.3	59.4 ± 0.1	66.3 ± 0.3	77.8 ± 0.4	52.8

LO: Lung Opacity, CM: Cardiomegaly, PL-T: Pleural Thickening, AE: Aortic Enlargement,
PF: Pulmonary Fibrosis, TB: Tuberculosis, PE: Pleural Effusion, Agg: Macro Average

B.3 Dependence on training dataset size

Here, we vary the diversity and size of the training dataset used for RAD-DINO by systematically enriching it with more diverse examples, such as out-patient studies. This incremental addition of data enables comparison with different baseline methods that use paired image–text datasets. Despite a performance drop compared to using the full dataset (as in Tables 1a and B.1), we observe that the RAD-DINO model trained with smaller-scale data (MIMIC-CXR: 197k), maintains its superior performance over baseline approaches trained with image–text contrastive learning demonstrated in Tables 1a and B.1 without requiring text input for training. Additionally, RAD-DINO is competitive to MRM [7] when trained with a similar sized dataset (see Figure B.2) but because RAD-DINO does not require paired image–text data, performance continues to scale with additional training data. For consistency with other ablation studies, we used the same backbone model, benchmark, and metric. Given that models tend to overfit with smaller dataset sizes, early stopping is applied by monitoring the validation loss computed on the CANDID-PTX classification task via linear probing.

For up to 546k samples, only the frontal chest X-ray scans (AP/PA) are utilised, as we empirically observe these to yield the maximal gain, given that the test set is composed exclusively of frontal images (see Figure B.2). Similarly, the inclusion of the PadChest [88] dataset provides an additional performance boost, due to the increased diversity of findings in out-patient datasets. In the final stage, lateral scans and an additional private dataset are utilised to observe how the presented approach scales with increased dataset quantities.

C Further analysis on model behaviour and results

C.1 Impact of image resolution on subtle findings

We also extend our resolution ablation studies, reported in Appendix B.1, to include subtle findings like pneumothorax and chest tubes using the CANDID-PTX dataset [39]. As detailed in Figure C.1, the results reveal that the RAD-DINO encoders’ performance diminishes at lower resolutions due to the ambiguity and loss of detail in the input images, highlighting the necessity of high resolution for accurately detecting such nuanced findings. In comparison to other baseline methods like BiomedCLIP and BioViL-T, the image-only pretrained RAD-DINO encoder demonstrates consistently superior performance across various resolutions (224 and 512 pixels, respectively). This suggests that RAD-DINO’s effective utilisation of higher resolutions could lead to a better performance in downstream tasks such as VQA and text generation, surpassing encoders trained at smaller resolutions [9, 10]. Furthermore, analysing results across different findings helps understand the impact of input resolution.

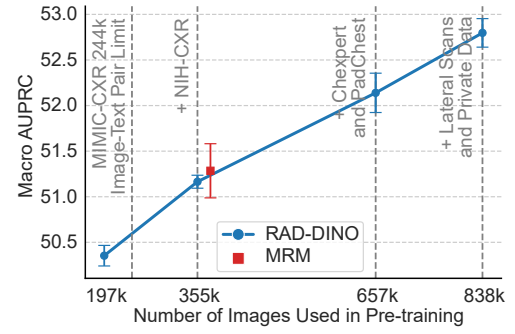


Figure B.2: Linear probing performance on VinDr-CXR vs number of training images used in RAD-DINO pre-training. Data is presented as mean \pm standard deviation.

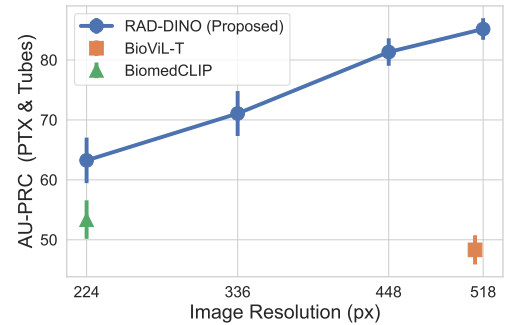


Figure C.1: Linear probing results for pneumothorax and chest tubes obtained on the CANDID-PTX dataset [39], for different image resolutions. Both pre-training and inference settings are adapted for the given input resolution. Data is presented as mean \pm standard deviation.

Table C.1: Lateral chest X-ray linear classification results obtained on the PadChest dataset with frozen backbone networks. Here we report mean and standard deviation of AUPRC results over five runs with different random seeds.

Image encoder	Pre-trained with Laterals	PadChest [88] (AUPRC)				Agg
		Vertebral deg. changes	Pleural Effusion	Costophrenic angle blunting		
BioViL-T [36]	✗	57.12 ± 2.44	82.10 ± 2.36	69.69 ± 2.21	69.64	
BiomedCLIP [37]	✓	69.06 ± 1.24	90.60 ± 1.02	76.21 ± 2.92	78.62	
MRM [7]	✓	76.97 ± 1.75	96.45 ± 0.98	83.09 ± 2.85	85.50	
RAD-DINO	✓	80.33 ± 1.32	94.53 ± 0.95	83.57 ± 2.63	86.14	

C.2 RAD-DINO requires fewer segmentation annotations

Additional ablations are performed to understand few-shot transfer of image networks to segmentation tasks; as such, the experiments in Section 2.3 are repeated for the segmentation of left and right lungs, for varying number of manual annotations used for training. Figure C.2 shows that the few-shot transfer of baseline approaches (BioViL-T and BiomedCLIP) is worse than the vision-only pre-trained RAD-DINO encoder with a linear segmentation decoder [22]. We see lower variation in the Dice scores for RAD-DINO across increasing training dataset sizes, reaching near-optimal segmentation performance even with very few samples. The performance further improves when RAD-DINO is combined with a UPerNet decoder. This implies that large scale image-only pre-training can potentially reduce the need for densely annotated medical scans for downstream semantic segmentation applications, which require medical expertise and are time-consuming to collect.

C.3 Experiments with lateral chest X-ray scans

We hypothesise that image–text alignment can be challenging for lateral scans and radiology text data, as there is often limited mutual information shared between these two data modalities. Specifically, certain findings reported in radiology textual reports may not be visible in lateral scans, or they are assessable by relying solely on the frontal scans. In this context, image-only SSL techniques, such as RAD-DINO, can be a useful alternative to simultaneously learn a rich set of imaging features from both frontal and lateral imaging views during pre-training.

To this end, we used a subset of studies from the PadChest dataset, selecting only the lateral scans containing specific findings, and excluded these studies from RAD-DINO pre-training. The selection of findings was guided by the feasibility of detecting them solely based on the lateral scans, in order to reduce task ambiguity. For these reasons, the following findings were selected based on prior research work [44, 45] that demonstrate the unique value of lateral scans in identifying them: “vertebral degenerative changes” (VDC), “pleural effusion” (PE), and “costophrenic angle blunting” (CAB). The positive and negative class distribution of each binary task is kept balanced by randomly sampling negative lateral scans from the rest of the dataset. The total dataset size is 11.9k, and the dataset is split across train/val/test at 80/10/10% for each random allocation by subject identifier. Since not all class labels were present for each image in this dataset, a subset of the dataset was used for the testing of models for each finding: N = 373 for VDC, N = 542 for PE, and N = 503 for CAB.

The results in Table C.1 indicate that BioViL-T performs nearly comparably to a random classifier on previously unseen findings, such as VDC, likely because it was predominantly trained with frontal scans from MIMIC-CXR. In contrast, the training dataset of BiomedCLIP includes a more balanced mix of frontal and lateral scans. In conclusion, we observe that approaches based on masked modelling, such as MRM and RAD-DINO, consistently deliver strong classification results. This demonstrates the effectiveness of the MIM objective in adapting to various imaging views. RAD-DINO can achieve this performance without requiring text supervision during pre-training.

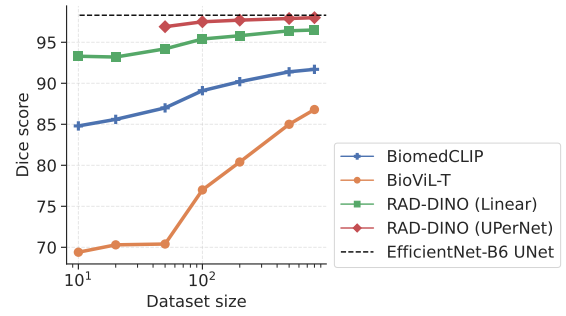


Figure C.2: Mean Dice score of right and left lungs vs. number of training images. EfficientNet-B6 UNet is trained end-to-end with all images to set the upper bound. The other approaches use either a linear or UPerNet decoder head on top of a frozen encoder backbone.

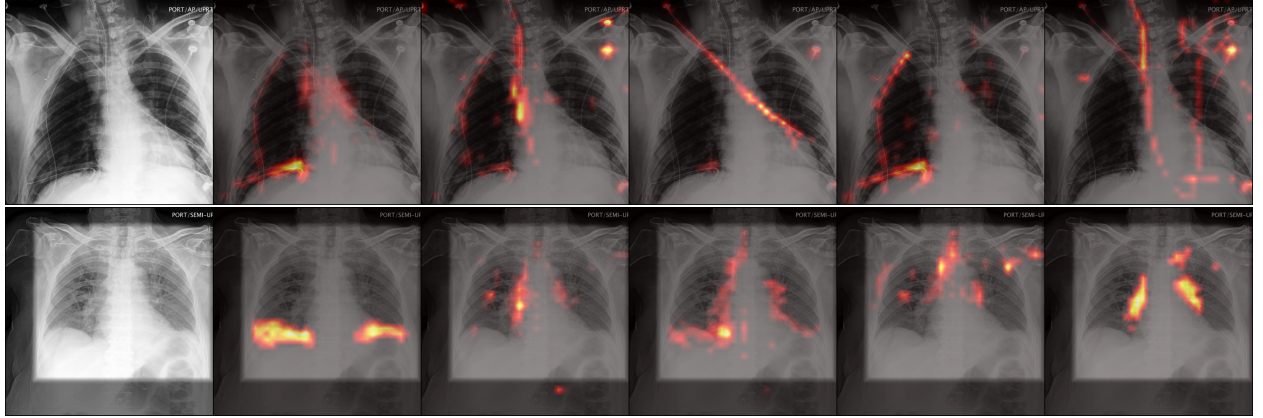


Figure C.3: Self-attention of the [CLS] token with respect to patch tokens are visualised for a subset of heads ($N=5$) from the last layer of RAD-DINO’s vision transformer. The network is trained without any explicit supervision and the attentions are computed without any gradient information for a specific target class as in the case of attention roll-out. The top row shows that RAD-DINO can locate each instance of support devices with high precision. Similarly, the bottom row is showing a chest X-Ray scan of a subject with pleural effusion and opacities; we see that the attentions are concentrated within the lung fields including the base and hilar regions.

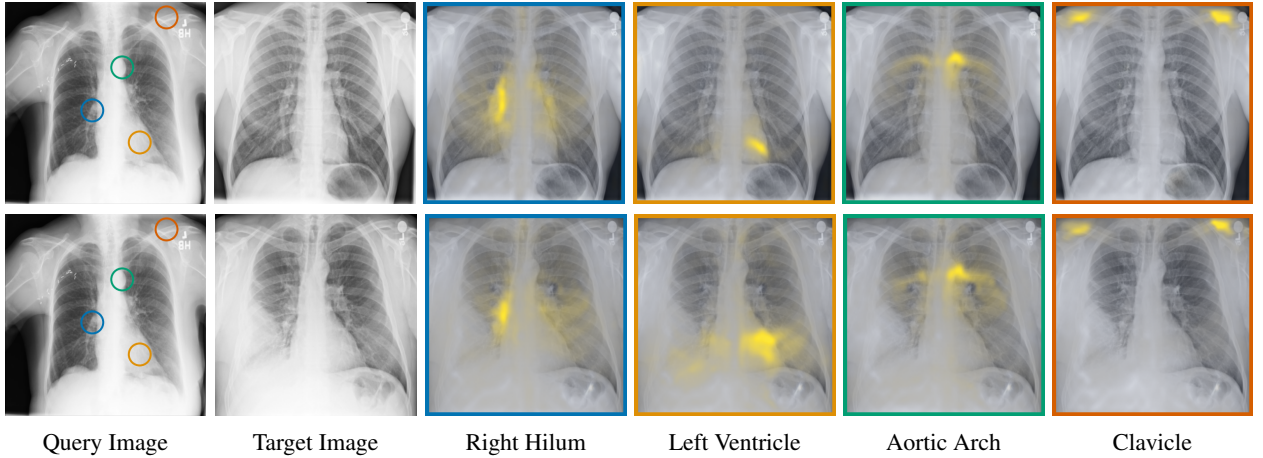


Figure C.4: Patch embedding similarities between pairs of chest X-ray images (one pair in each row), computed with RAD-DINO, with respect to four different landmark points (marked with circles on the left-most source image for demonstration purposes). For a given landmark point on the query image, its similarity to the patch embeddings of the target image is highlighted in yellow and proportional to the heatmap brightness. We observe that the anatomical correspondences between images from different subjects are learnt during pre-training.

C.4 Qualitative results

C.4.1 Visualisation of self-attentions

Figure C.3 shows the self-attention of the [CLS] token with respect to patch embeddings extracted with the RAD-DINO encoder. The top row demonstrates RAD-DINO’s ability to accurately attend and trace different types of support devices. The bottom row shows that on images with pleural effusion and opacities, attention heads are concentrated within the lung fields including the base and hilar regions.

C.5 Patch embedding correspondences

Figures C.4 and C.5 provide additional qualitative examples of patch embedding matching between pairs of chest X-ray images collected from different subjects. In particular, we see that the anatomical correspondences (Figure C.4) are well preserved despite the presence of findings such as loculated right pleural effusion.

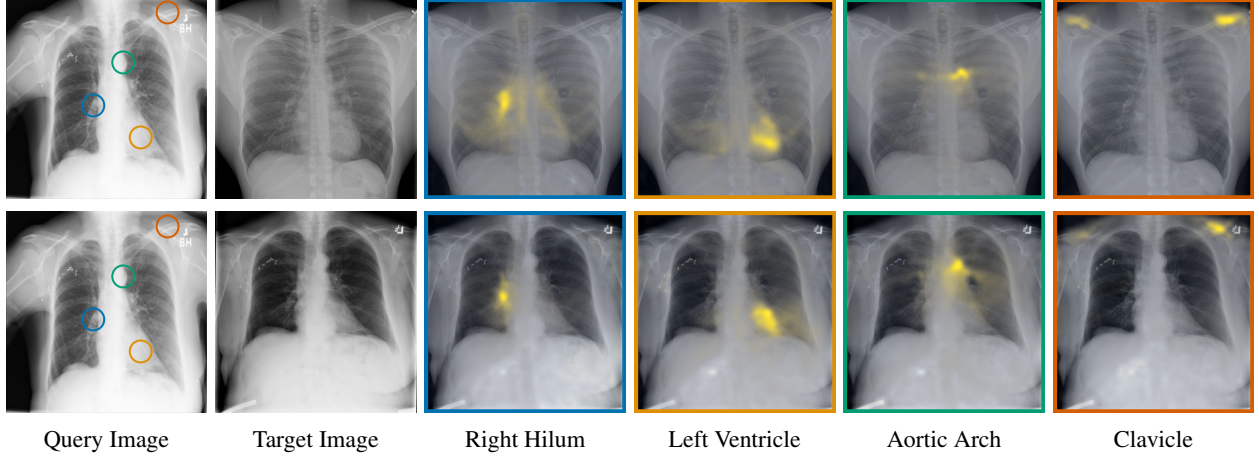


Figure C.5: Patch embedding similarities between pairs of chest X-ray images (one pair in each row), computed with RAD-DINO, with respect to four different manually picked landmark points (marked with circles on the left-most source image for demonstration purposes). For a given landmark point on the query image, its similarity to the patch embeddings of the target image is highlighted in yellow and proportional to the heatmap brightness. We observe that the anatomical correspondences between images from different subjects are learnt during pre-training.

Similarly, local patch embeddings for abnormal findings such as consolidation and nodules can be well aligned across scans, see Figure 2. We also observe that when there is an overlap between an anatomical region and an abnormal finding (e.g., pleural effusion in the costophrenic angle), the nearest-neighbour match between anatomically corresponding points is affected. This leads to embeddings that capture both types of information simultaneously.

C.5.1 Qualitative segmentation results

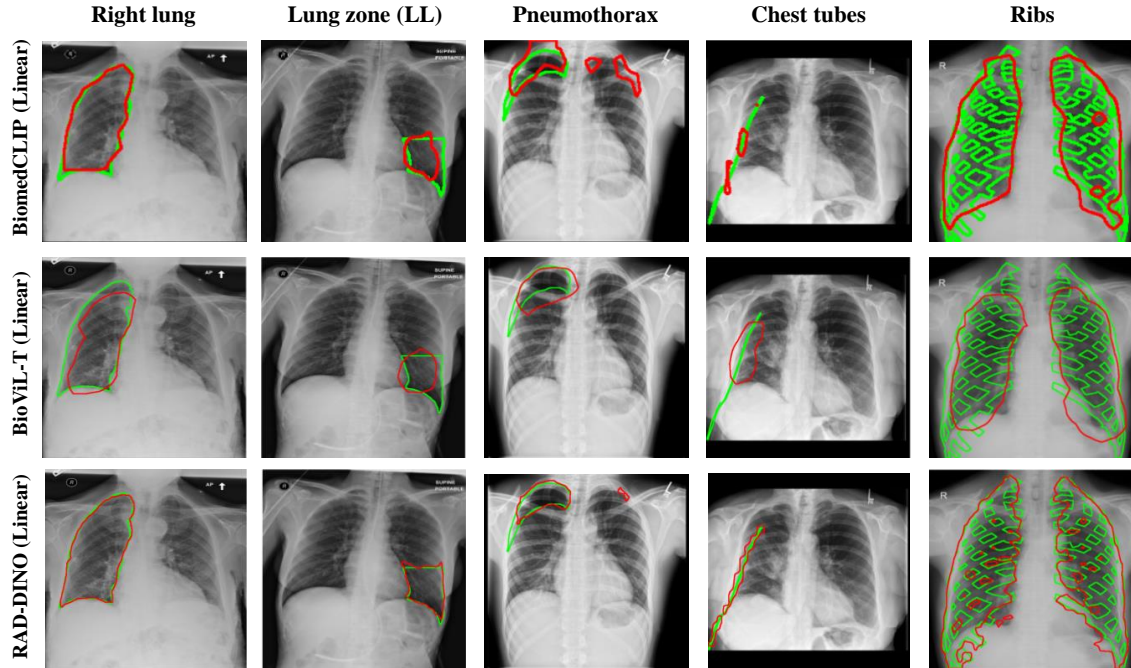
The qualitative results using the pre-trained RAD-DINO encoder are notably better for all tasks, compared to the image-text contrastively trained encoders BioViL-T and BiomedCLIP using a linear decoder head (Fig. C.6a). Specifically, we see more detailing of shapes and edges for the RAD-DINO predicted segmentation mask (more prominently seen in smaller structures such as chest tubes and lung zones). In contrast, the fine-grained edge and shape details are not preserved in the masks predicted by both BioViL-T and BiomedCLIP. The segmentation masks produced by BiomedCLIP show disconnected components (similar to OpenCLIP segmentation qualitative results in [22]). Moreover, the segmentation masks predicted using the RAD-DINO encoder with a UPerNet decoder preserve fine-granular details of each structure and are close in visual quality to the masks predicted by the best-performing segmentation model EfficientNet-B6 UNet (Fig. C.6b).

C.6 Bias and fairness

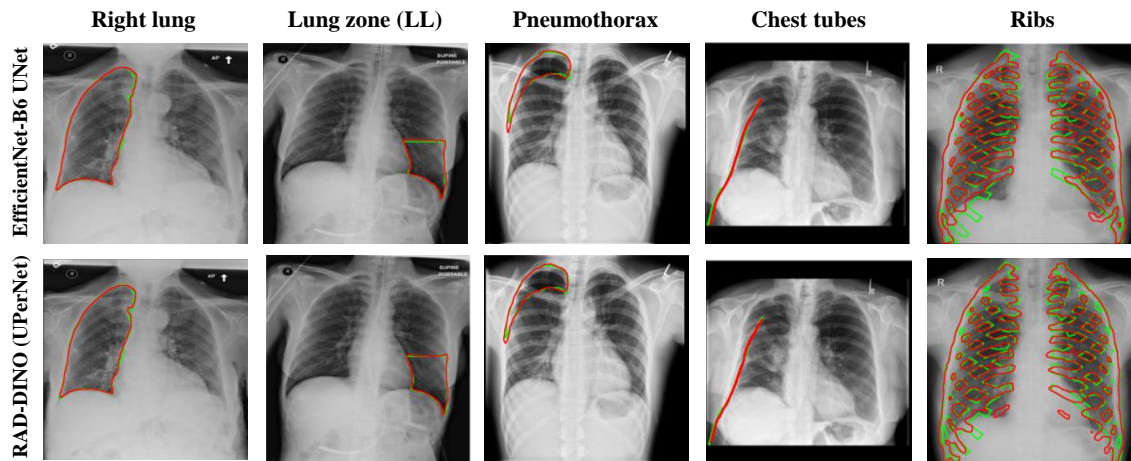
In this section, we replicate the experiments done in Section 3.6, focusing on ethnicity. We select a subset of the MIMIC-CXR dataset ($N = 60.1k$) where the radiology reports indicated “no findings” to minimize potential confounding between metadata and pathologies. We then link the anonymised subject information with the medical records provided in the MIMIC-IV dataset. A single-layer classifier is trained on features extracted from frozen backbones to predict one of the following classes: ‘white’, ‘asian’, ‘black/african american’, ‘hispanic/latino’, ‘american indian/alaska native’, ‘other’. We perform 5-fold cross-validation and reported the accuracy as ‘mean (standard deviation)’. Consistent with the results on sex, age, weight, and BMI in Table 5, we find that RAD-DINO outperforms BiomedCLIP and BioViL-T in predicting ethnicity, see Table C.2.

Table C.2: Linear classification of ethnicity labels with frozen backbone networks. We perform 5-fold cross validation and report ‘mean (standard deviation)’ accuracy.

Encoder	Ethnicity
BioViL-T [36]	64.8 (0.2)
BiomedCLIP [37]	64.6 (0.1)
RAD-DINO	76.9 (0.5)



(a) Qualitative segmentation results for BiomedCLIP, BioViL-T and RAD-DINO encoders with linear decoder head.



(b) Comparing qualitative results between the best two segmentation models, namely RAD-DINO (UPerNet) and EfficientNet-B6 UNet.

Figure C.6: Qualitative results for semantic segmentation tasks on chest X-rays (green: ground truth mask, red: predicted mask) (LL: left lower).

As discussed in [126], it is unclear whether ethnicity can be causally inferred from X-ray images. [126] demonstrate that ethnicity predictions are nearly random when controlling for other metadata variables like ‘age’ and ‘sex’, which have clear causal relationships with image features in the X-ray. As previously shown in Table 5, RAD-DINO is superior to the baseline methods when it comes to predicting metadata. In line with these findings, RAD-DINO is also the best model for predicting ethnicity. To address concerns about how the stronger discriminative power of RAD-DINO might influence the fairness of models built upon it, we perform a stratified analysis of our results on lung segmentation (Table 3) and report generation (Table 2).

C.6.1 Segmentation

We compute the average Dice score for each of the groups ‘white’, ‘asian’, ‘black/african american’, ‘hispanic/latino’, ‘american indian/alaska native’, ‘other’ in the test set. Table C.3, we report the average dice across all ethnicities and the worst group dice. We find that the difference between the average dice and the worst group dice is similar for all three encoders. The worst group for all encoders is ‘white’, which is also the largest group, likely due to the highest variance. Since we only have ethnicity information for the MIMIC dataset, we perform the analysis for the lung and lung zones segmentation task.

Table C.3: Semantic segmentation results obtained with linear head [22] on top of frozen backbone networks. Dice scores are reported as mean across the dataset. “Lungs” denotes the separate segmentation of the left and right lungs, while “Lung zones” signifies the segmentation of six distinct lung zones. The average Dice score is reported for both scenarios.

Encoder	Decoder	Lungs avg	Lungs worst	Lung zones avg	Lung zones worst
BioViL-T [36]	Linear	83.2	81.4	69.4	66.2
BiomedCLIP [37]	Linear	90.4	89.9	76.0	73.1
RAD-DINO	Linear	95.9	95.6	85.7	82.1

C.6.2 Report generation

For the report generation experiments in Table 2, we compute the average Rouge-L for each of the groups ‘white’, ‘asian’, ‘black/african american’, ‘hispanic/latino’, ‘american indian/alaska native’, ‘other’ in the test set. In Table C.4, we report the average accuracy across all ethnicities and the worst group accuracy. We found that all three encoders perform worst for the ‘asian’ subgroup, where all three encoders show a similar drop of about 7 to 8 points.

In conclusion, while RAD-DINO is better at predicting the ethnicity (or respectively correlated variables [126]) of a patient than the other image encoders, we do not observe any signs of decreased fairness in its performance.

Table C.4: Downstream radiology report generation results obtained on the official test split of MIMIC-CXR dataset ($N=2,461$). The same set of image encoders are used in conjunction with a two-layer MLP projector and Vicuna-7B (v1.5) [50] as LLM to generate the Findings section from given input images.

Encoder	ROUGE-L avg	ROUGE-L worst
BiomedCLIP [37]	23.1	16.6
BioViL-T [36]	23.5	16.3
RAD-DINO	24.6	16.6

D Dataset details

D.1 RAD-DINO pre-training

To train the RAD-DINO image encoder, we use a combination of chest X-ray datasets that are outlined in Table D.1. The BRAX dataset [90] consists of 24,959 high-quality digital chest radiography studies acquired prior to the COVID-19 pandemic from 19,351 patients from a large general Brazilian hospital. Being sourced from a Brazilian hospital, BRAX can help address the under-representation of certain populations in medical datasets. MIMIC-CXR [17] consists of chest X-ray studies including radiology reports collected from intensive care unit (ICU), where a subset of clinical findings are observed. It has been the main pre-training data resource in prior art [5, 36, 7]. Similarly, ChestX-ray14 [87] is compiled

Table D.1: Imaging datasets (Multi-CXR) used for the continual pre-training of RAD-DINO. Note that for some datasets only a subset of subjects are included to exclude the evaluation set from the pre-training dataset.

Dataset	View	Patient cohort	Number of subjects	Number of images
BRAX [90]	frontal, lateral	all available in institutional PACS	19,351	41,620
CheXpert [56]	frontal, lateral	inpatient and outpatient	65,240	223,648
MIMIC-CXR [17]	frontal	ICU	188,546	210,491
ChestX-ray14 [87]	frontal	not specified	32,717	112,120
PadChest [88]	frontal, lateral	all available	67,000	160,817
Private	frontal, lateral	outpatient	66,323	90,000
Total			439,177	838,336

by the NIH and is composed of chest X-ray scans from more than 30,000 patients, including many with advanced lung disease. PadChest [88] consists of medical images along with their associated reports of subjects reporting at San Juan Hospital (Spain), where the reports were labelled with 174 different radiographic findings, 19 differential diagnoses, and 104 anatomic locations organised as a hierarchical taxonomy. Since the PadChest dataset is comprised of studies collected from both in- and out-patient wards, its diversity is quite valuable in generalising to findings seen outside the ICU settings. Note that lateral scans are not excluded from RAD-DINO training although evaluations heavily assess the findings seen on frontal scans. Lastly, we utilise a set of in-house chest X-ray imaging dataset collected from outpatient clinics to further assess the scalability RAD-DINO model with training dataset size.

In summary, the large-scale combined pre-training dataset comprises of chest X-ray images obtained from subjects with diverse reported radiological findings, collected from different patient cohorts across different geographical locations and time durations. All images are used for pre-training from the given datasets, except MIMIC-CXR [17] where their recommended training split is used.

D.2 Downstream evaluation tasks

For the image classification task, we use VinDr-CXR [35], CANDID-PTX [39], and RSNA-Pneumonia [40]. The VinDr-CXR subset for the six reported findings consists of 18,000 images from the same number of subjects. CANDID-PTX [39] contains 19,237 images from the same number of subjects. RSNA-Pneumonia [40] contains 26,684 images from the same number of subjects. For the semantic segmentation task, we train and evaluate the encoder-decoder networks for left and right lungs, lung zones, pneumothorax, chest tubes, and ribs. For lung and lung zone segmentations, lung masks are provided in a lung segmentation dataset based on MIMIC-CXR [75]. To extract lung zone masks from lung masks, bounding boxes for six lung zones (left upper, left mid, left lower, right upper, right mid, right lower) are obtained from the Chest Imagenome dataset [63] based on MIMIC-CXR. Corresponding chest X-ray images are directly extracted from the MIMIC-CXR database [17]. The lung and lung zone segmentation datasets contain 1,138 images from the same number of subjects. For pneumothorax and chest tubes, we use the chest X-ray images and masks from CANDID-PTX [39] consisting of 19,237 images from the same number of subjects. The VinDR-RibCXR dataset [76] consists of rib segmentations for 20 ribs (L1-L10, R1-R10) of images collected from 245 subjects.

E Implementation details

E.1 RAD-DINO pre-training

We train the RAD-DINO encoders on 4 compute nodes of 4 NVIDIA A100 GPUs each. To pre-train the RAD-DINO encoder (ViT-B/14), we use a training batch size of 640 (40 per GPU), the AdamW optimizer, base learning rate 0.001 and a cosine learning rate scheduler with linear warmup. For an input image of size 518×518 , we generate a global view by extracting a random crop with a size sampled from $\mathcal{U}(259, 518)$, and upsampling it back to 518×518 . For local views, we use $\mathcal{U}(104, 259)$ and upsample to 196×196 . The encoder is trained for 100 epochs. More details including augmentations are provided in Section 3.

We trained a RAD-DINO encoder only on publicly available datasets and shared the model weights¹ on Hugging Face, along with detailed instructions to facilitate further research by the community. On Hugging Face, we added a model card for the trained RAD-DINO model and shared the list of all the images used for RAD-DINO training.

¹<https://huggingface.co/microsoft/rad-dino>

E.2 Baseline image encoders

The source code and pretrained weights of the baseline image encoders were obtained from public resources: CLIP@224¹, CLIP@336², BioViL-T³, BiomedCLIP⁴, MRM⁵, and DINOv2⁶. For each baseline, we used its corresponding image preprocessing pipeline and image inference implementation, if provided. If a network used a special token, such as [CLS], during pre-training for contrastive learning, it is used in linear probing experiments for better baseline performance. For the MRM baseline, we observed better downstream performance when probing was applied on the pooled patch embeddings, which were used for both masked image and text modelling objectives during pre-training. Since the baseline evaluations focused on interpreting single images, the BioViL-T model was evaluated in static mode, rather than in a temporal analysis of two consecutive scans.

E.3 Downstream evaluation tasks

The implementation details for the training and evaluation of each downstream network presented in Section 2 are provided below:

E.3.1 Image classification

We evaluate the classification tasks on 1 compute node of 8 NVIDIA V100 GPUs. We use a training batch size of 96 (12 per GPU), AdamW optimizer, base learning rate 5×10^{-5} , and a cosine learning rate scheduler. We use the following preprocessing and augmentations: centre-cropping and resizing (518×518 for all encoders except BiomedCLIP and CheXzero, where we resize to 224×224), random horizontal flip, random cropping, random affine transform, random colour jittering, and random Gaussian noise. For the RAD-DINO experiments, we normalise the intensities using statistics computed from all images in MIMIC-CXR [17]. The classification models are trained for 100 epochs. The last checkpoint is selected for inference on the test set as we did not observe overfitting while monitoring the validation loss. We perform 5-fold cross-validation and report the mean and standard deviation of AUPRC.

E.3.2 Semantic image segmentation

We evaluate the segmentation tasks on 1 compute node of 8 NVIDIA V100 GPUs. We use a training batch size 80 (10 per GPU), Adam optimizer, base learning rate 5×10^{-4} , and a cosine learning rate scheduler. We use the following preprocessing and augmentations: centre-cropping and resizing (518×518 for all encoders except BiomedCLIP and CheXzero where we resize to 224×224), random horizontal flip (except left-right lungs and lung zones), random affine transform, elastic transform, random brightness and contrast jittering, and random gamma adjustments. For RAD-DINO experiments, we normalise the intensities using statistics computed from all images in MIMIC-CXR [17]. The segmentation models are trained for 100 epochs. We use a 70/15/15 split by subjects for train, validation and test sets, respectively, and report metrics on the test set (for ribs segmentation, we use the provided data splits, i.e., 196 train, 49 test). The model with minimum loss on the validation set is used for inference on the test set. For the given GPU setup, training a linear head on top of the RAD-DINO encoder takes 0.60 seconds/iteration, whereas training a UPerNet decoder takes 0.66 seconds/iteration.

E.3.3 Textual report generation

Training is performed on compute nodes of 4 NVIDIA A100 GPUs with 80GB RAM. We use the same hyperparameters set in LLaVa-1.5 [49]. Namely, we use a batch size of 128 (32 per GPU), and a cosine learning rate scheduler with warmup during 3% of the training steps, and base learning rate 2×10^{-5} . We only perform single-stage fine-tuning for three epochs, where the image encoder is frozen while the LLM, along with the adaptor, are updated. Finally, we use 32-bit full precision for decoding up to 150 tokens with a batch size of 1 during inference.

E.3.4 Experiments with patient demographics

First, we select a subset of the MIMIC-CXR dataset where the radiology reports noted “No findings”. We then link the anonymised subject information with the medical records provided in the MIMIC-IV dataset. The resulting dataset

¹<https://huggingface.co/openai/clip-vit-large-patch14>

²<https://huggingface.co/openai/clip-vit-large-patch14-336>

³<https://huggingface.co/microsoft/BioViL-T>

⁴https://huggingface.co/microsoft/BiomedCLIP-PubMedBERT_256-vit_base_patch16_224

⁵<https://github.com/RL4M/MRM-pytorch>

⁶<https://github.com/facebookresearch/dinov2>

Variable	Range	N (thousands)
Age (years)	< 20	0.8
	20–40	11.1
	40–60	23.2
	60–80	20.4
	> 80	4.6
Weight (kg)	< 50	2.7
	50–65	11.3
	65–80	17.9
	80–95	14.2
	> 95	13.8
BMI (kg/m^2)	< 18.5	1.9
	18.5–25	17.4
	25–30	18.8
	30–35	11.4
	> 35	10.4

Table E.1: Binned distributions of continuous variables for the experiment described in Section 3.6

consists of 60.1k images with AP/PA view. Second, we compute the embeddings for BioViL-T, BiomedCLIP, and RAD-DINO. Third, we train a logistic regression model to predict the demographics variables: sex, age, weight and BMI using the image embeddings. The model is evaluated using five-fold cross-validation with an 80/20 split and trained for 100 epochs with default settings (we used the LogisticRegression module from scikit-learn [127]). Sex was a binary variable with categories Female (N = 29.3k) and Male (N = 30.8k). The continuous variables, age, weight, and BMI, were discretised into five bins each (Table E.1).